POLITECNICO DI TORINO
Repository ISTITUZIONALE

A Custom Genetic Algorithm Framework for Early-Stage Optimization of Electromechanical Actuators

Original
A Custom Genetic Algorithm Framework for Early-Stage Optimization of Electromechanical Actuators / Levati, M., Bertolino, A.C., Guida, R., Migliore, D.F., Finamore, E., Sorli, M.. - In: ACTUATORS. - ISSN 2076-0825. - ELETTRONICO. - 15:2(2026), pp. 1-34. [10.3390/act15020099]

Availability:
This version is available at: 11583/3008489 since: 2026-03-10T09:20:48Z

Publisher:
Multidisciplinary Digital Publishing Institute (MDPI)

Published
DOI:10.3390/act15020099

Terms of use:

This article is made available under terms and conditions as specified in the corresponding bibliographic description in the repository

Publisher copyright

(Article begins on next page)

20 November 2026

actuators

MDPI

Article

A Custom Genetic Algorithm Framework for Early-Stage Optimization of Electromechanical Actuators

Michelangelo Levati [1,*], Antonio Carlo Bertolino [1], Roberto Guida [1], Domenico Fabio Migliore [2], Edoardo Finamore [2] and Massimo Sorli [1]

[1] Dipartimento di Ingegneria Meccanica e Aerospaziale (DIMEAS), Politecnico di Torino, 10129 Torino, TO, Italy; antonio.bertolino@polito.it (A.C.B.); roberto.guida@polito.it (R.G.); massimo.sorli@polito.it (M.S.)
[2] Leonardo S.p.A., 10146 Torino, TO, Italy; domenico.migliore@leonardo.com (D.F.M.); edoardo.finamore@leonardo.com (E.F.)
* Correspondence: michelangelo.levati@polito.it

Abstract

This work presents a systematic methodology for the preliminary design and optimization of electromechanical actuators, aimed at minimizing overall mass and rotational inertia while satisfying torque and speed requirements. The proposed approach integrates dimensionless scaling relationships, derived and corrected from catalog data, with a genetic algorithm that performs multi-parameter optimization across different actuator architectures. The algorithm enables the exploration of non-linear and multi-modal design spaces, allowing the identification of balanced solutions between mechanical efficiency and dynamic performance, employing custom functions for individual generation, constraint handling, and compatibility verification to ensure feasible and consistent architecture designs throughout the optimization process. A case study on the steering system of an aircraft nose landing gear illustrates the method's ability to define optimal design parameters in real mechanical systems. Linear and non-linear dynamic analyses confirmed the compliance of the optimized design with control and stability requirements. The study demonstrates how the developed custom constrained genetic optimization approach can effectively support the early design phase, reducing the computational effort required in further stages and improving the overall consistency of electromechanical actuator development.

Keywords: electromechanical actuator; preliminary sizing; preliminary design; genetic algorithm; scaling laws; nose landing gear

Check for updates

Academic Editor: Giorgio Olmi

Received: 19 December 2025
Revised: 20 January 2026
Accepted: 2 February 2026
Published: 4 February 2026

Copyright: © 2026 by the authors. Licensee MDPI, Basel, Switzerland. This article is an open access article distributed under the terms and conditions of the Creative Commons Attribution (CC BY) license.

1. Introduction

Today, electromechanical actuators (EMAs) are widely used in various fields, such as industrial automation, aeronautics, robotics, and electric mobility. These actuators convert electrical energy into mechanical motion, either linear or rotary, enabling precise control of position, velocity, and force/torque. In various application contexts, EMAs are considered a more advantageous alternative to pneumatic and hydraulic actuators due to their ability to be easily integrated with digital control and monitoring systems, their higher energy efficiency under steady-state conditions, and their reduced infrastructural complexity [1,2].

Despite constraints in managing impulsive overloads and their capacity for passive energy dissipation, EMAs provide enhanced precision in motion control and more straightforward predictive diagnostics owing to their inherent integration with sensors and controllers [3]. The lack of pressurized fluids and the more compact design simplify

installation, lower operational costs, and improve operational safety, especially in situations that are sensitive to contamination or have stringent hygiene standards [4,5].

In addition to static and dynamic performance considerations, an important aspect in the design and implementation of EMAs concerns their stability and long-term operational reliability. The stability of an actuator system depends on its capacity to preserve controllable and predictable behavior under external disturbances, load variations, and non-linearities within the electromechanical drive and control system. In EMAs, the use of high-resolution feedback systems and advanced digital controllers helps mitigate many of the dynamic instabilities typical of electromechanical architectures. In terms of reliability, EMAs offer significant advantages over their fluid-dynamic counterparts, thanks to the absence of fluid leakage, the reduction in wear-prone components, and the possibility of continuous monitoring of operational parameters through integrated sensors [6,7].

The sizing of EMAs is essential to ensure that the required performance and reliability are maintained over time and that the life-cycle maintenance cost is reduced. Over the years, various approaches have been developed to support the preliminary design of EMAs, each differing based on the level of abstraction adopted, the specific application context, and the availability of initial data. The first set of methods adopts a top-down perspective, focusing on high-level architectural definition and preliminary sizing. These approaches are particularly suited for complex, redundant, or distributed systems—characteristics often found in the aeronautical sector, where systemic integration is a central design requirement [8,9]. Alongside these high-level methods, simulation-based techniques have gained prominence for their ability to evaluate performance, structural limitations, and functional criticalities early in the design process. These tools provide essential feedback for refining design choices before moving into detailed development phases [10,11]. Other studies take a more functional or kinematic perspective, showing that established optimization techniques—originally developed for conventional aircraft systems—can still be effectively applied in the context of EMAs [12]. At the same time, some approaches explore the detailed analysis of the electromechanical chain, modeling the integrated design of the motor, linear actuator, and external load dynamics [13]. Within this framework, symbolic modeling techniques have proven useful in guiding the selection of key components, such as motor–gearbox combinations, based on system requirements [14]. More recently, advanced top-down strategies have been proposed for control-oriented design, further reinforcing the importance of systemic thinking from the earliest stages of EMA development [15].

In many of these studies, scaling laws or similarity laws (SLs) are employed to compare different types of actuators. The use of SLs is often more cost-effective than bottom-up design or the use of FEM or multiphysics simulations, especially in the preliminary stages of design. SLs enable reliable estimates of key parameters, such as torque, mass, power and efficiency, to be obtained quickly from existing actuators and components. In contrast, bottom-up design requires detailed analysis and a long development time, while numerical simulations require high computational resources and a very accurate initial data set. SLs thus offer an excellent compromise between accuracy, speed and cost, ideal for feasibility studies and pre-dimensioning. Indeed, SLs are widely used in various fields, such as mechanics, hydraulics, and micro-systems, to compare different types of actuators and components. Over the past two decades, several contributions have studied the application of SLs for the analysis and optimization of electromechanical components such as motors, gearboxes, clutches, and transmission systems. An example is the optimization of the rotor arrangement (internal and external) of permanent-magnet motors based on the required torque [16]. Following this, it is possible to produce SLs for the main components of EMAs, enabling preliminary design decisions to be guided through symbolic modeling frameworks [11,17,18].

This study delineates a novel, comprehensive approach for identifying the optimal EMA design, focusing on the minimization of mass and moment of inertia based on torque and rotational speed system requirements. Specifically, the use of a genetic algorithm (GA) to compare possible configurations and preliminary designs of the EMA, with verification of requirements through a linear and a non-linear model, is presented. GAs offer a particularly advantageous approach due to their ability to efficiently explore large and non-linear search spaces without the need for gradient information or simplified models [19]. Inspired by natural selection, GAs work with a population of potential solutions, evolving them through selection, crossover, and mutation over successive generations. The GAs' stochastic nature is ideal for the constrained multi-objective problems of mechanical optimization, allowing them to escape local minima and find global optima.

As validation, a case study is conducted in the aviation field, considering the ever-growing phenomenon of "More Electric Aircraft", which proposes the replacement of traditional pneumatic and hydraulic actuators with EMAs. In this context, the shift to electric systems offers significant advantages in terms of efficiency and weight reduction [20,21], enhancing the overall performance of the aircraft as well as the operational reliability, and simplification of maintenance [22]. In the current work, the workflow is applied to an aircraft nose landing gear (NLG) steering system, which is used as a practical case study for demonstrating the optimization process.

Some studies have further explored the potential of EMAs in aircraft actuation systems [23,24], suggesting that their integration for the steering system can reduce the overall weight of the aircraft while improving operational efficiency [25].

The application of EMAs in specific contexts, such as thrust control systems of landing gear, has also been analyzed in relation to forced feedback systems, which improve stability and safety during movement control [26,27]. The use of EMAs has also been considered for the steering system of the NLG in several studies. Some studies present methodologies for selecting the main components of the EMA for the NLG steering system based on a limited number of inputs [10,11]. Others have analyzed the differences between various types of transmission, observing the impact they have on steering system performance [28,29], including for configurations with two actuators [30]. Other studies give special attention to safety and reliability when selecting EMA components [8,9].

This article is organized as follows. In Section 2 the following topics are presented: the description of the workflow; the methods used to define the system requirements; identification of candidate architectures; the approach for defining the relevant SLs; and finally, the non-convex method for identifying the optimal architecture. Section 3 discusses: the requirements imposed as a function of the aircraft specifications for the case study; the SLs defined for the identified components and the correction of the curves by fitting to the catalog data; the tuning of the algorithm parameters used and the results, both of the case study and as the input data vary; and the verification by frequency analysis of the results obtained. Section 5 provides an overview of the presented work, with particular attention to the results obtained and possible future implementations.

2. Materials and Methods

This section presents the methodology used for the workflow, and the logical steps are shown in Figure 1.

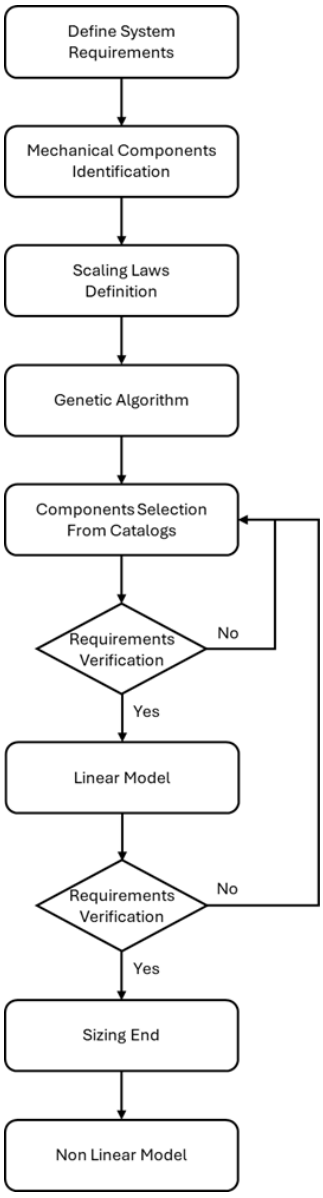


Figure 1. EMA preliminary design workflow.

The process starts with the definition of the system-level requirements, including structural, functional, and integration constraints, as well as the specific performance criteria for the EMA. Following these two phases, the next stage involves identifying different EMA architectures and the components that can be used for them, depending on criteria previously defined.

At this point, SLs are derived to mathematically characterize the attributes of the candidate components. The SLs, together with the established requirements, are incorporated into a GA improved with custom verification functions. In the present work, the algorithm iteratively explores the design spaces, identifying candidate architecture and components that represent an optimal solution in terms of mass and inertia. After identifying an optimal solution, components are selected from the catalogs, and a verification of the predefined requirements is performed.

The data of the selected components are then used to create a linear model, which varies depending on the components chosen. This model is used to verify key dynamic performance metrics, such as stability, frequency response, and control system design. The process returns to the component selection phase if they are not met, opting for components

with similar characteristics and enhanced performance. Otherwise, the process of sizing is considered successfully completed, and a preliminary non-linear model of the EMA can be produced. With this, the system prerequisites can be tested under more realistic operating conditions.

2.1. EMA Components

EMAs can be divided into two main types based on the type of motion they produce, depending on the transmission system. Linear actuators convert the rotary motion of the motor into linear motion through a mechanical drive mechanism. Rotary actuators maintain the rotary motion of the motor and transmit it to other moving parts.

Generally, an EMA consists of a motor, a speed reducer, a motion transmission system, and possibly electromagnetic brakes or clutches.

The motor is the component responsible for converting electrical energy into mechanical motion. Depending on the specific requirements of the application, it may be a direct current (DC), alternating current (AC), or stepper motor. The first transmission stage is a speed reducer designed to reduce the motor's rotational speed while increasing the torque transmitted to the output. The clutch functions as a mechanism to temporarily disengage the motor from the load, providing protection to the system from critical overload events. The brake maintains the actuator in a fixed position when required. The second transmission stage conveys mechanical motion from the previous stages to the actuator's output, and it may incorporate gears, belts, or shafts.

2.2. Scaling Laws for EMA Components

SLs are mathematical formulations that characterize the variations in component parameters by the variation in geometric dimensions. In the mechanical component sizing context, SLs are widely used to establish the relationship between structural and physical or dynamical parameters of a component, such as torque, speed, mass and moment of inertia.

In this work, the convention used for SLs denotes the scaling ratios by X^*, representing the ratio between the parameter X_{com} of a component and the corresponding parameter X_{ref} of the reference component, as defined in Equation (1) [31].

$$X^* = \frac{X_{com}}{X_{ref}} \tag{1}$$

Each EMA component has characteristic SLs, which can be obtained through different approaches [11]. A combination of the Buckingham theorem approach and the direct approach was used in the present work.

In this work, SLs are defined based on the fundamental relationships between the nominal torque of the component and other parameters of interest. The results are validated using the curves produced with the corresponding catalog parameters.

In particular, the generic SL of the generic component parameter X_i^* can be expressed as an a–power function of its nominal torque T_i. In order to correct curves described by SLs and to ensure a better fit for the catalog trends, the SL is multiplied by the coefficient k_i, as given in Equation (2).

$$X_i^* = k_i T_i^{*a} \tag{2}$$

The correction coefficient is optimized with respect to the catalog data, using a function to minimize the Root Mean Squared Error between the estimated and predicted values.

2.3. Non-Convex Optimization Selected

The selection of components for EMAS requires evaluation of both the system's technical specifications and the adopted analysis method. Since multiple components are involved, such as the motor, gearbox, clutch, and transmission, the resulting optimization problem may present a complex landscape of solutions characterized by different local minima. In such scenarios, conventional gradient-based optimization techniques may prove inadequate, making non-convex algorithms a more suitable approach [19,32].

Among non-convex optimization strategies, GAs are widely employed in mechanical engineering. Inspired by natural evolution, GAs address complex optimization problems by iteratively evolving a population of candidate solutions [33–35]. Through mechanisms such as selection, crossover, and mutation, a GA progressively enhances the solution quality to find the global optimum. The classic iterative process of a GA is shown in Figure 2a. Figure 2b shows the modification proposed and used in this paper, based on the compatibility of the components with each other and with the system requirements.

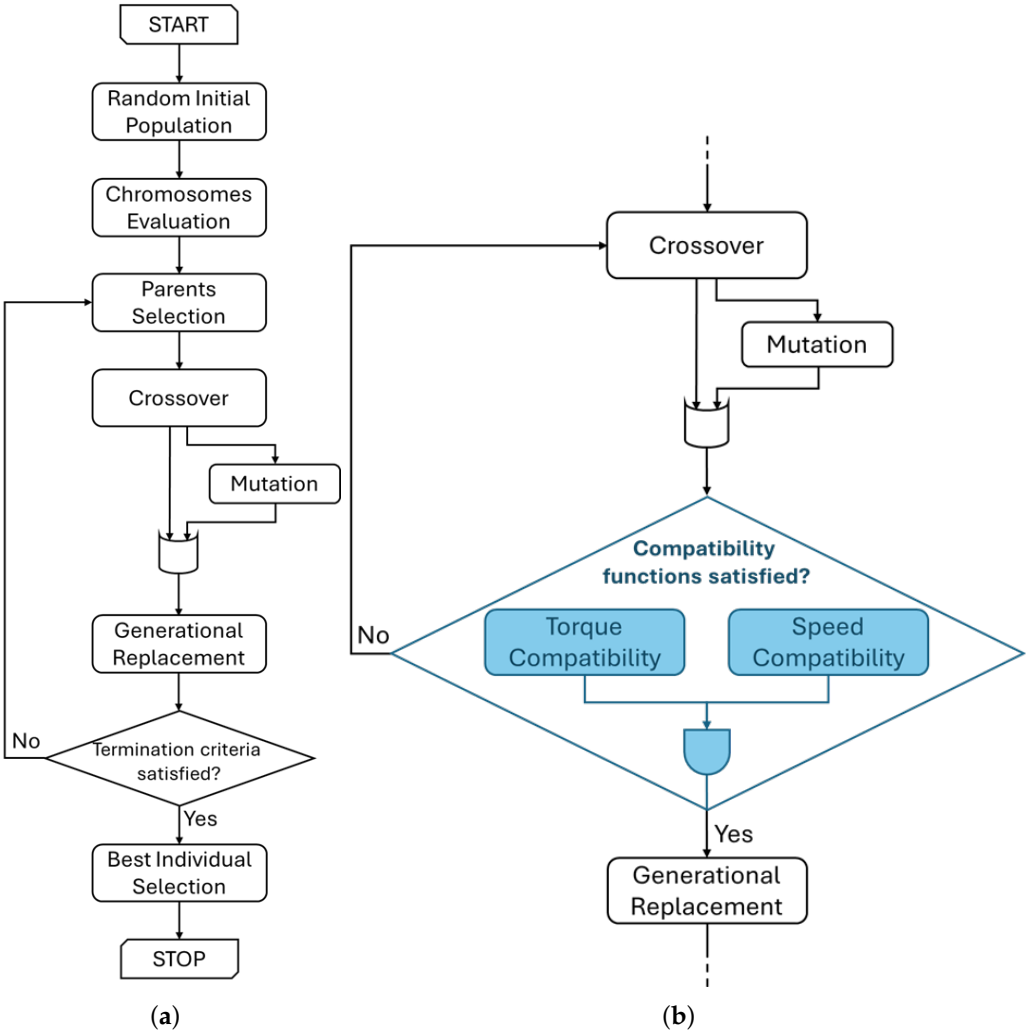


Figure 2. Genetic algorithm flow chart. (**a**) Classic flow chart. (**b**) Proposed modification to flow chart.

2.3.1. Individual Characterization

The individuals are described by a chromosome, a sequence of genes, encoded as parameter vectors $[u_1; \ldots; u_i; \ldots; u_n]$, whose values determine the properties of the EMA system. The genes used for the current work are listed in Table 1.

Table 1. EMA genes used for the genetic algorithm to identify the individual with the best combination of mass and inertia.

Symbol	Gene	Unit
u_1	EMA output torque	Nm
u_2	Gearbox gear ratio	–
u_3	Max steering angle	deg
u_4	Min steering speed	deg/s
u_5	Driven helical gear tooth number	–
u_{6rs}	Roller screw lead	mm
u_{6wg}	Worm screw thread number	–
u_{6hg}	Pinion helical gear tooth number	–

Some genes are common to all configurations, while others are specific to configurations. This is because different types of transmission include components characterized by different properties that affect SLs. Specifically, configurations that include a roller screw depend on the lead of the roller screw u_{6rs}; those that include a worm gear depend on the number of threads in the gear u_{6wg}; and configurations with two helical gears are affected by the number of teeth in the pinion u_{6hg}.

For each EMA configuration, the initial population consists of a randomly generated set of individuals. Each individual represents a potential solution. In cases where it is not possible to reach the number of individuals designated for the initial population, the algorithm will make further attempts to complete the filling. If the target initial population number still cannot be reached, but there are viable individuals, the configuration will not be discarded. However, a flag will be triggered that will take into account the small number of individuals, which may lead to a suboptimal solution for that configuration at the end of the planned generations. Conversely, if not even one individual can be identified, the configuration will be discarded.

This is because attempting to optimize a configuration that is unable to meet the requirements for any individual in its population would lead to a loss of computational time.

Throughout the generation of each individual, whether in the initial population or subsequent iterations, the proper transmission of speed and torque is ensured across components while accounting for efficiency losses and transmission ratios. Thus, component compatibility is ensured.

With regard to speed constraints, each component must operate within its predefined performance limits. Validation begins with the motor and proceeds through the transmission chain, ensuring that the transmitted speed does not exceed the maximum speed allowed by every component. Furthermore, depending on the architecture, the output rotational speed is computed based on gear ratios. Any individual that fails to meet the required performance criteria is excluded from the population.

Torque consistency is verified in reverse, starting from the output torque and working back through the mechanical chain, up to the motor. If at any point the transmitted torque exceeds the maximum capacity of the component, the individual is excluded.

2.3.2. Individual Fitness Based on Mass and Moment of Inertia

In optimization problems, fitness f is a function that evaluates the quality of a candidate solution according to certain criteria.

Unlike traditional approaches that focus only on mass minimization [34], this work proposes a fitness evaluation criterion that simultaneously accounts for both the mass M and moment of inertia J. This is because the total moment of inertia has a direct influence on the EMA's dynamic response and system stability.

In the present work, the moment of inertia of the EMA components J_{EMA} and the moment of inertia of the load J_{load} are considered. The load is the NLG itself. Both moment-of-inertia contributions are referred to the motor shaft, according to an arbitrarily defined convention. They are combined to provide a total equivalent moment of inertia J_{tot}.

The fitness function integrates both mass and inertia through a weighted criterion, thereby allowing a more balanced evaluation of candidate solutions.

To ensure that the mass and the moment of inertia can be fairly compared, both have been normalized. This normalization process makes the two values comparable. Thus, individual fitness is evaluated as the sum of the normalized mass $\bar{M}_{EMA}$ and moment of inertia $\bar{J}_{tot}$, each multiplied by its respective weight w_m and w_j, as shown in Equation (3).

$$f = \bar{M}_{EMA} w_m + \bar{J}_{tot} w_j \tag{3}$$

The weights w_m and w_j allow the relative influence of each parameter to be balanced according to the specific needs of the case study. This flexible approach makes it possible to emphasize mass or inertia reduction according to design priorities, avoiding suboptimal solutions that would result from considering only a single optimization objective. The weight assigned to the parameters depends on the application case and design specifications that vary according to the field of application.

In fitness optimization, the dynamic performance and efficiency of the EMA are not considered, as they are not defined as objects of minimization for this work. However, a posteriori checks are carried out to analyze their correct sizing.

2.3.3. Parent Selection, Crossover and Generational Turnover

There are several types of selection for identifying the best individuals, including: Roulette Wheel Selection, Tournament Selection, Rank-Based Selection, and Plus Selection; similarly, the type of crossover can be: Single-point Crossover, Multi-point Crossover, Blend Crossover, and Simulated Binary Crossover [36].

In the present work, Rank-Based Selection is used for parent selection. This method involves assigning higher ranks to individuals with lower fitness. Unlike Roulette Wheel Selection, which assigns selection probabilities proportional to absolute fitness, Rank-Based Selection mitigates the risk of premature convergence by preventing a few highly fit individuals from dominating the selection process [37].

To enhance variability in solution exploration, a probability of being selected is assigned to each individual based on its rank. Compared to Tournament Selection, this approach maintains increased selective pressure control, ensuring balance between exploration and exploitation while avoiding the risk of frequently selecting less prominent individuals [38].

A constraint is imposed to prevent the same parent from being used for the generation of more than one offspring, reducing the likelihood of premature convergence to a local minimum.

Blend Crossover (α-BLX) is used to combine parents in the present work. This type of crossover generates new individuals by selecting genes in an extended range relative to their parents, favoring genetic diversity more than SBX, which tends to keep offspring close to their parents [39]. In addition, α-BLX is better suited to optimization problems with continuous variables, such as the one we are considering, as opposed to the single-point and multi-point methods, which are better suited to problems with discrete solutions [40].

In α-BLX the offspring genes are generated as a linear combination of the parent genes. For each gene, a real number u_i is selected from an interval that extends beyond the parent, as in Equation (4) [36].

$$u_i \in \left[\min(x_{i_{(t)}}; y_{i_{(t)}}) - \alpha\, d,\ \max(x_{i_{(t)}}; y_{i_{(t)}}) + \alpha\, d\right] \tag{4}$$

$$\text{with} \quad d = |x_{i_{(t)}} - y_{i_{(t)}}| \tag{5}$$

where d is the distance between the two parent genes $x_{i_{(t)}}$ and $y_{i_{(t)}}$; the α coefficient regulates the width of the interval and must be positive. An α value of 0.2 is used.

To increase genetic variability and avoid stagnation of the algorithm, a mutation mechanism is also used. The new individual gene is selected from between the boundary values of the corresponding gene when mutation occurs.

In particular, the inverse annealing approach is used, as it is useful in multiple-continuous-variable problems [36]. This method involves an initial step of decreasing the mutation probability P_m, followed by a gradual increase in the final generations, as shown in Equation (6). In the following equation, g corresponds to the generation in which the individual is generated, and G_{max} is the maximum number of expected generations.

$$P_m = P_{m_{\max}} - \left|\sin\left(\frac{\pi\, g}{G_{\max}}\right)\right| (P_{m_{\max}} - P_{m_{\min}}) \tag{6}$$

Constant mutation can lead to rapid convergence to suboptimal solutions, whereas inverse annealing ensures that there is still sufficient genetic variation in the advanced stages of the algorithm [38].

During the generation of each individual, component compatibility checks are performed. This step is carried out using functions that analyze the rotation speeds and torque transmitted between each component. Incompatible individuals are discarded during generation, which continues until the predetermined turnover value is reached. A parameter regulates the number of attempts that can be made to generate each individual before considering the two parents incompatible for the generation of a new individual.

It is also essential to check the compatibility of the individual with the application case. In particular, as with the components, it is verified that the torque and rotation speed obtained at the EMA output meet the requirements imposed.

A bottom-up method is used to perform these two verifications. Specifically, during the generation of the individual components, the minimum torque and minimum rotation speed required for the most downstream component are imposed. After that, the kinematic chain is traced back, verifying that each component is capable of withstanding a torque and rotation speed at least equal to that of the component further downstream.

The replacement of individuals with offspring is done by Tournament Selection. The use of Tournament Selection for offspring replacement promotes competition within groups, in which only the most promising individuals survive, but at the same time it ensures genetic diversity in the population, giving individuals with higher fitness a chance to survive [36].

3. Results and Discussion

This section presents and analyzes the results obtained from the application of the workflow applied to the study case of the aircraft NLG steering system.

3.1. Case Study Scenario

The NLG steering system design must meet several requirements for proper operation and to ensure safety, accuracy, and reliability during landing, take-off, and taxing [41].

The EMA must provide sufficient torque T_{NLG} to steer the wheel through the full steering angle without requiring forward movement of the aircraft or asymmetric thrust of the electric motor. Steering torque sizing must be accomplished in a stationary aircraft condition, when the friction force on the wheels is maximum.

For aircraft taxing operations, it is necessary to define a maximum steering angle θ_{max} of the NLG, which characterizes the choice of EMA architecture. However, steering capability must be reduced to a smaller angle during landing and take-off phases to ensure aircraft stability and minimize the risk of skidding, especially on wet or icy surfaces. In addition to the taxing maximum steering angle θ_{tax} and the landing and take-off maximum steering angle $\theta_{lan/toff}$, the minimum steering speed ω_{min} of the NLG must be defined. Generally, this range varies in the range 5–60 deg/s, depending on the aircraft type [41].

NLGs are typically equipped with an anti-shimmy device consisting of a damper, designed to reduce the shimmy effect, which primarily occurs during the landing phase.

In some cases, in addition to the shimmy damper, EMA control is used to compensate for the shimmy effect, operating at higher frequencies. In this work, it was decided not to perform compensation, but to verify that the shimmy frequency does not resonate with the natural frequencies of the system.

The aircraft construction and environmental data used for the present work corresponds to data for a medium-sized transport aircraft and is summarized in Table 2. The data were derived from the available information on the Douglas DC-6 (C-118) aircraft [42].

Table 2. Case study aircraft construction and environmental parameters from Douglas DC-6 aircraft [42].

Symbol	Parameter	Value	Unit
M_A	Aircraft mass	48.000	kg
M_{NLG}	Nose landing gear mass	300	kg
h_{NLG}	Nose landing gear height	1.70	m
e	Wheel displacement	0.07	m
R_o	Tire free radius	0.26	m
s	Tire thickness	0.23	m
–	NLG load percentage	12	%
μ	Road friction coefficient	0.8	–

In particular, the steering system is sized to withstand the maximum steering torque associated with aircraft operation under full-load conditions, i.e., with a mass of 48.000 kg. This assumption reflects a conservative approach to sizing and defines the reference operating conditions adopted for the design of the actuator. Based on the available data from the Douglas DC-6 case study shown in Table 2 [42], it is possible to derive the necessary requirements for the steering system. The requirements taken into consideration in the current choice of architecture are given in Table 3.

Table 3. Case study on nose landing gear steering system requirements of Douglas DC-6 [41,42].

Symbol	Parameter	Value	Unit
T_{NLG}	Required steering torque	5.000	Nm
θ_{tax}	Taxing NLG steering angle	±45	deg
$\theta_{lan/toff}$	Landing and take-off NLG steering angle	±1.5	deg
ω_{min}	Minimum NLG steering speed	25	deg/s
f_{EMA}	Position cutoff frequency	4	Hz

A schematic representation of the NLG of the present case study is shown in Figure 3. In particular, an "L" configuration is used. This configuration is used for the NLG because of its high dynamic stability and neutral static stability [43].

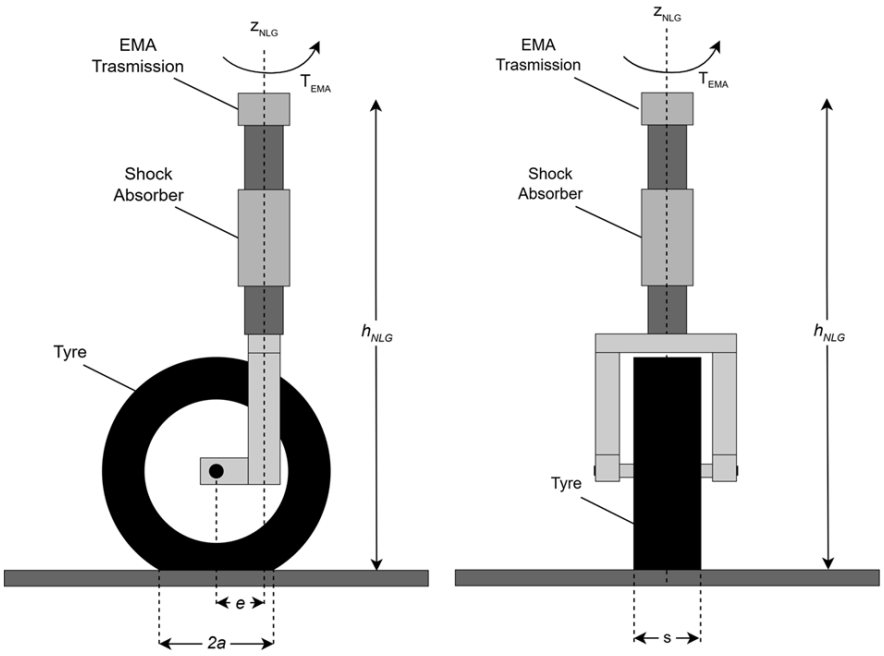


Figure 3. Schematic representation of the nose landing gear with an "L" shape. (**a**) Lateral view. (**b**) Front view.

Steering Torque Estimation for Stationary Aircraft

To define the steering torque required by the EMA, it is necessary to analyze the resistant torque T_{NLG} that opposes the rotation. In stationary conditions, the resistant torque depends on the friction force F_f between the wheel and the ground, as well as on the contact area caused by the compression of the wheel against the ground due to the weight force on the NLG $F_{z_{NLG}}$.

The vertical force acting on the NLG $F_{z_{NLG}}$ can be estimated as part of the total weight force of the aircraft [41]. The safety standards require the weight force $F_{z_{NLG}}$ acting on the NLG to be between 6% and 20% of the total weight of the aircraft; a preferable range would be 8% with, e.g., the aft center of gravity, increasing to 12% with, e.g., the forward center of gravity [44].

In the current work, the limiting case of a load on the NLG equal to 12% of the total load is considered. The vertical force $F_{z_{NLG}}$ can then be derived from Equation (7).

$$F_{z_{NLG}} = \frac{(L_{tot} - L_{NLG})}{L_{tot}} M_A g = 0.12 M_A g \tag{7}$$

where M_A is the aircraft mass, L_{tot} is the distance between the NLG and MLGs along the aircraft's x-axis, and L_{NLG} is the distance between the NLG and the CoM.

The aircraft tire can be considered similar to a toroid, with thickness s, free radius R_o and loaded radius R_L, due to the flattening h of the wheel to the ground, as shown in Figure 4.

As a result, the vertical force is distributed over the elliptical contact surface of the tire A_e, generating an average pressure P_e, as expressed in Equation (8).

$$P = \frac{F_{z_{NLG}}}{A_e} = \frac{4F_{z_{NLG}}}{2\pi as} \tag{8}$$

where a is the half contact length of the tire. The curvature of the tire is taken into account when calculating the half contact length, resulting in an 85% reduction in the apparent contact length c.

$$2a = 0.85 \cdot c = 0.85 \cdot 2\sqrt{R_0^2 - R_L^2} \tag{9}$$

R_0 represents the free radius of the wheel, and R_L the radius of the wheel under load.

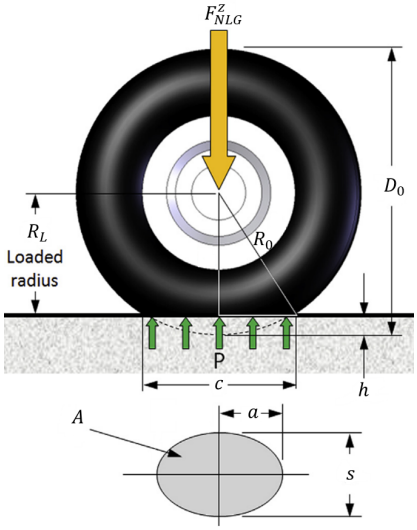


Figure 4. A schematic diagram of the tire [43].

Assuming an evenly distributed specific ground pressure on the tire as the mean pressure on the contact area P, a coefficient of friction between the tire and ground μ, and an infinitesimal contact area dA distant l from the point O_1, as shown in Figure 5, the infinitesimal frictional moment $d\,T_{NLG}$ can be estimated with Equation (10).

$$dT_{NLG} = \mu P l dA = \mu \frac{F_{z_{NLG}}}{\pi 2as} l dA \tag{10}$$

Assume O_1 as the rotation point, corresponding to the projection of the Z-axis of the NLG and shifted by a distance equal to the wheel arm e from the center of the wheel O_0, with $e < a$, and s as the tire thickness, as shown in Figure 5. It is possible to estimate the value of the NLG frictional moment T_{NLG} by integrating $d\,T_{NLG}$ on the contact surface in a similar way to that reported for the car model [45].

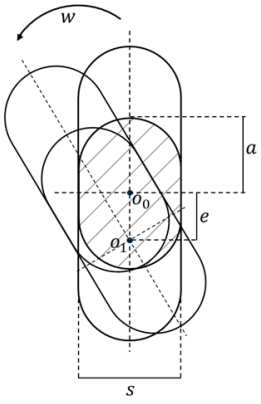


Figure 5. Schematic diagram of tires rotating around the Z-axis of the NLG.

To simplify the integral, it is possible to use polar coordinates and consider the rectangular surface that circumscribes the contact ellipse. The pressure is assumed to be uniformly distributed over the rectangle, with a ratio between the elliptical and rectangular surfaces of $\pi/4$. Thus, the NLG frictional moment can be estimated by using Equation (11).

$$\begin{aligned} T_{NLG} = & 2\int_0^{\operatorname{atan}\left(\frac{2(a-e)}{s}\right)} \int_0^{\frac{s}{2\cos(\theta)}} \frac{\mu F_{z_{NLG}}}{2as} r^2 \, dr d\theta \\ & + 2\int_0^{\operatorname{atan}\left(\frac{2(a+e)}{s}\right)} \int_0^{\frac{s}{2\cos(\theta)}} \frac{\mu F_{z_{NLG}}}{2as} r^2 \, dr d\theta \\ & + 2\int_0^{\operatorname{atan}\left(\frac{s}{2(a-e)}\right)} \int_0^{\frac{s}{2\sin(\theta)}} \frac{\mu F_{z_{NLG}}}{2as} r^2 \, dr d\theta \\ & + 2\int_0^{\operatorname{atan}\left(\frac{s}{2(a+e)}\right)} \int_0^{\frac{s}{2\sin(\theta)}} \frac{\mu F_{z_{NLG}}}{2as} r^2 \, dr d\theta \end{aligned} \tag{11}$$

3.2. EMA Candidate Configurations

EMAs are integrated systems combining an electric motor, a mechanical transmission, and control electronics to generate precise and controllable motion. Their design can vary significantly depending on performance requirements, leading to multiple possible configurations that differ in motor topology, speed reduction mechanism, and transmission type [10,20,29].

Both frameless brushless motors and conventional permanent-magnet synchronous motors (PMSMs) represent viable choices for EMAs. Annular motor topologies, which typically feature a higher pole count and a larger effective air-gap radius, offer increased torque density and reduced rotor inertia. These characteristics make them particularly suitable for applications requiring high precision and dynamic performance. Conversely, cylindrical PMSMs, generally designed with fewer poles, are capable of achieving higher rotational speeds but tend to exhibit lower torque per unit volume. Nevertheless, the actual performance of either topology ultimately depends on the specific electromagnetic and mechanical design.

Different technologies can be used for the speed reducer, including planetary, harmonic, or cycloidal reducers. The choice between these solutions depends on the required speed reduction and efficiency. The selection of an appropriate reduction mechanism depends on the desired trade-off between speed reduction, torque transmission, and dimensional constraints. Harmonic drives provide high reduction ratios with compact size and good precision. On the other hand, planetary reducers are more robust [46]; they can be easily scaled due to their modular stage-based construction, and they can have higher transmission ratios. One of the main advantages of cycloidal gears is their high resistance to shock loads and ability to transmit high torques with relatively compact dimensions.

The clutch allows for locking motion in case of failure or enables free rotation under specific operating conditions. Only one type of clutch is used because it does not impose weight changes on the other components since it does not directly affect the magnitude of the torque and speed transmitted.

Motion transmission to the load can be achieved through ball and roller screws or different gear types, such as worm gears or helical gears, depending on the precision requirements and the force to be transmitted. Roller screws are often used in aerospace applications due to their efficiency and ability to handle high loads while maintaining precise positioning. An alternative frequently considered for motion transmission is the use of worm gears, which are particularly advantageous in applications requiring high speed reduction and self-locking. Helical gears, on the other hand, are used only in

configurations that require having the motor axis along an axis parallel to that of the NLG due to construction requirements, as they are heavier and bulkier as solutions.

Configurations using two parallel motors can also be used to reduce the load on each motor and to introduce an extra degree of redundancy [30]. In this paper, the considered configurations assume the use of a single motor, but the process can be extended to multi-motor configurations.

By combining the various components identified, a total of 18 possible EMA configurations can be obtained from the combination of all components listed in Table 4. To identify the configurations, acronyms are used, composed of the components' abbreviations in the order Motor–Reducer–Transmission. The clutch abbreviation is not mentioned because only one type is used. All component abbreviations are also shown in Table 4.

Table 4. EMA components and corresponding abbreviations.

Motor		Reducer		Clutch	Transmission	
Type	**Code**	**Type**	**Code**	**Type**	**Type**	**Code**
Annular	A	Planetary	P	Electromagnetic	Helical Gear	H
Cylindrical	C	Cycloidal	C	dual flow	Worm Gear	W
		Harmonic	H		Roller Screw, Rack, & Driven Gear	R

3.3. Scaling Laws with Correction Coefficient for Selected Components

Tables 5–9 show the SLs, obtained with the Buckingham theorem approach. The parameters are expressed as a function of the nominal torque T or force F.

Table 5. Scaling laws for DC brushless annular and AC brushless cylindrical motors [11].

Parameter	**Unit**	**Cylindrical Motor**	**Annular Motor**	**Equation**
Nominal Output Torque	Nm	T^*	T^*	
Mass	kg	$M^* = T^{*3/3.5}$	$M^* = T^{*2/3}$	(12)
Length	m	$l^* = T^{*1/3.5}$	$l^* = T^{*1/3}$	(13)
Diameter	m	$d^* = T^{*1/3.5}$	$d^* = T^{*1/3}$	(14)
Moment of inertia	kg m^2	$J^* = T^{*5/3.5}$	$J^* = T^{*4/3}$	(15)
Max allowed speed	rpm	$\omega^* = T^{*-1/3.5}$	$\omega^* = T^{*-1/3}$	(16)
Maximum allowed torque	Nm	$T^*_{max} = T^*$	$T_{max} = T^*$	(17)

Table 6. Scaling laws for planetary, cycloidal and harmonic speed reducers [11].

Parameter	**Unit**	**Planetary Gearbox *n* Stages**	**Cycloidal & Harmonic 1-Stage Speed Reducer**	**Equation**
Nominal Output Torque	Nm	T^*	T^*	
Mass	kg	$M^* = T^*$	$M^* = T^*$	(18)
Length	m	$l^* = T^{*1/3}$	$l^* = T^{*1/3}$	(19)
Diameter	m	$d^* = T^{*1/3}$	$d^* = T^{*1/3}$	(20)
Moment of inertia	kg m^2	$J^* = T^{*5/3}$	$J^* = T^{*5/3}$	(21)
Max allowed speed	rpm	$\omega^* = T^{*-1/3}$	$\omega^* = T^{*-1/3}$	(22)
Maximum allowed torque	Nm	$T^*_{max} = T^*$	$T^*_{max} = T^*$	(23)

Table 7. Scaling laws for clutches [11].

Parameter	Unit	Clutch	Equation
Nominal Output Torque	Nm	T^*	
Mass	kg	$M^* = T^{*3/4}$	(24)
Length	m	$l^* = T^{*1/3}$	(25)
Diameter	m	$d^* = T^{*1/3}$	(26)
Moment of inertia	kg m^2	$J^* = T^{*5/4}$	(27)
Max allowed speed	rpm	$\omega^* = T^{*-1/3}$	(28)
Maximum allowed torque	Nm	$T^*_{max} = T^*$	(29)

Table 8. Scaling laws for roller screw and racks [11].

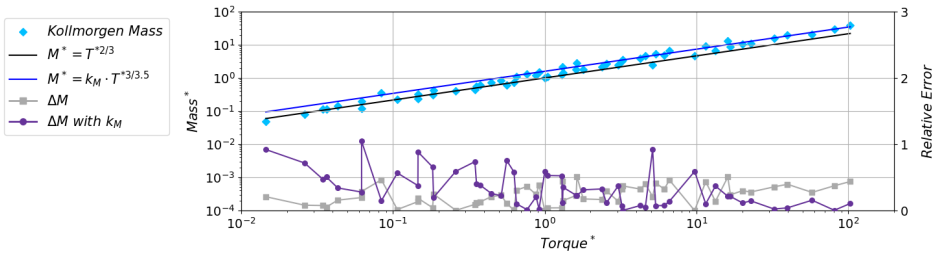
Parameter	Unit	Roller Screw	Rack	Equation
Nominal Output Force	N	F^*	F^*	
Mass	kg	$M^*_n = F^{*3/2}$ (nut)	–	(30)
Mass per unit length	kg/m	$M_l = F^*$ (screw)	$M^*_l = F^*$	(31)
Nominal diameter	m	$d^* = F^{*1/2}$	–	(32)
Moment of inertia	kg m^2	$J^*_n = F^{*5/2}$ (nut)	–	(33)
Moment of inertia per unit length	kg m	$J^*_l = F^{*2}$ (screw)	$J^*_l = F^{*2}$	(34)
Maximum allowed output force	N	$F^*_{max} = F^*$	$F^*_{max} = F^*$	(35)

Table 9. Scaling laws for worm gears and helical gears [11].

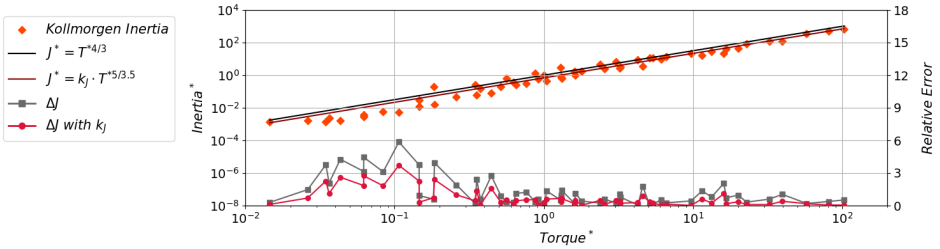
Parameter	Unit	Pinion or Wheel	Worm Gear	Equation
Nominal Output Torque	Nm	T^*	T^*	
Tooth Number	–	Z^*	Z^*	
Mass	kg	$M^* = T^* \cdot Z^*$	$M^* = T^*$	(36)
Width	m	$h^* = T^{*1/3} \cdot Z^{*-1/3}$	$h^* = T^{*1/3}$	(37)
Nominal diameter	m	$d^* = T^{*1/3} \cdot Z^{*2/3}$	$d^* = T^{*2/3}$	(38)
Moment of inertia	kg m^2	$J^* = T^{*5/3} \cdot Z^{*7/3}$	$J^* = T^{*5/3}$	(39)
Max allowed speed	rpm	$\omega^* = T^{*-1/3}$	–	(40)
Maximum allowed output torque	Nm	$T^*_{max} = T^*$	$T^*_{max} = T^*$	(41)

Figure 6 shows the mass and moment of inertia SL curves obtained from Tables 5–9 and the corresponding corrected curves with the k_i correction parameter. Curves are compared to the catalog data, and the difference between the relative errors ΔJ and ΔM, with and without the correction coefficient, is shown.

In Figure 6a, the cyan rhombuses represent catalog data of the mass M^* over the torque T^*; the straight lines represent the M^* scaling laws without and with the correction coefficient, respectively in black and blue; masses' relative errors ΔM between theoretical and catalog values are shown at the bottom, with light gray squares for data without correction and purple circles with correction. Similarly, in Figure 6b, the orange rhombuses represent catalog data of the inertia J^* over the torque T^*; the straight lines represent the J^* scaling laws without and with the correction coefficient, respectively in black and crimson; relative errors ΔJ between theoretical and catalog values are shown at the bottom, with dark gray square for the data without correction and red circles with correction.



(**a**)



(**b**)

Figure 6. Scaling laws as a function of nominal torque T^* and their relative errors for frameless brushless motor [47]. (**a**) Scaling laws of mass M^*. (**b**) Scaling laws of moment of inertia J^*.

As can be seen, the improvement brought by the correction is particularly evident for the moment-of-inertia relative error, while for the mass relative error there is an overestimation for lower torque values and a more accurate estimate for intermediate and higher values. Overall, even for mass, the result can be considered acceptable.

In Table 10 is shown the comparison between the coefficients of determination R^2 for all the SLs described in Tables 5–9, both with and without the correction coefficients k_i of Equation (2).

Table 10. Comparison of coefficients of determination R^2 of mass, inertia and speed SLs of the EMA components, with and without correction coefficient. Theoretical data are compared with component catalogs [47–55].

Component	Coefficient of Determination—R^2					
	Mass		Inertia		Speed	
	Original	Corrected	Original	Corrected	Original	Corrected
Annular Motor	0.793	0.978	0.887	0.985	0.349	0.800
Cylindrical Motor	0.547	0.947	0.771	0.975	0.685	0.862
Planetary Reducer	0.963	0.963	0.780	0.937	0.429	0.821
Cycloidal Reducer	0.885	0.996	0.588	0.977	0.591	0.622
Harmonic Reducer	0.948	0.960	0.886	0.944	0.766	0.882
Clutch	0.432	0.798	0.141	0.819	0.706	0.723
Roller Screw	0.979	0.987	0.940	0.972	-	-
Helical Gear	0.716	0.961	0.520	0.970	-	-

This analysis confirms the validity of the proposed SLs if considering the correction coefficients, demonstrating good agreement between theoretical predictions and catalog data.

3.4. EMA Optimization via Genetic Algorithm

The GA is developed to compare different EMA configurations and select the optimal one for the case study. The optimization process has two main steps: initially, the algorithm is used to identify the best solution within each configuration, and then the optimal solu-

tions identified for the different configurations are compared with each other to determine the overall optimal solution.

3.4.1. GA Parameter Tuning

First it is necessary to choose the weights assigned to the parameters of the fitness function. In this work, $w_m = 0.8$ and $w_j = 0.2$ were chosen. This heuristic choice reflects the intent to prioritize actuator optimization from a mass-reduction perspective while still retaining a non-negligible contribution from inertia in the overall performance index. The weights were defined to enable a representative test of the optimization routine and were chosen to demonstrate the GA's ability to balance multiple objectives.

To ensure an optimal balance between exploration and exploitation, the choice of GA parameters shown in Table 11 is guided by a sensitivity analysis of the GA performance. The results shown below are related to the EMA configuration that includes an annular motor, a planetary reducer and a roller screw, rack and driven wheel.

Table 11. Parameters of the genetic algorithm used to identify the optimal architecture of the NLG EMA.

Parameter	Value
Initial population	150
Population turnover rate	0.20
Crossover type	α-BLX
Offspring gene α factor	0.2
Parent selection method	Rank-based
Duplicate parents	False
Maximum mutation rate	0.1
Minimum mutation rate	0.01
Discarded individual selection method	Tournament
Max number of generations	150
Population minimum delta fitness	0.0001
Mass weight rate	0.8
Inertia weight rate	0.2

Figures 7 and 8 show the results of the evolution of the best individual fitness f_b, the mean population fitness f_m and the delta population fitness δ_f over generations for different numbers of populations and turnover values, over different executions.

Figure 7 examines the influence of variation in population size between 50 and 300 individuals, while maintaining a fixed turnover rate equal to 0.20.

As can be seen, a larger population provides greater genetic diversity, delaying convergence and also allowing for deeper exploration of the search space. However, beyond a certain population threshold, the fitness improvement becomes marginal, on the order of 10^{-4}, indicating that a larger population does not significantly improve the quality of the solution, but increases the computational cost. From the shown results, it can be concluded that a value of 150 individuals in the population is the most suitable choice.

Analyzing the generations at which the δ_f thresholds are reached and the corresponding values of f_b in Figure 7 allows the optimal maximum number of generations to be determined. In particular, for generations greater than the 150th, the f_b improvement becomes marginal, on the order of 10^{-4}. Based on this analysis, the maximum number of generations was set to 150.

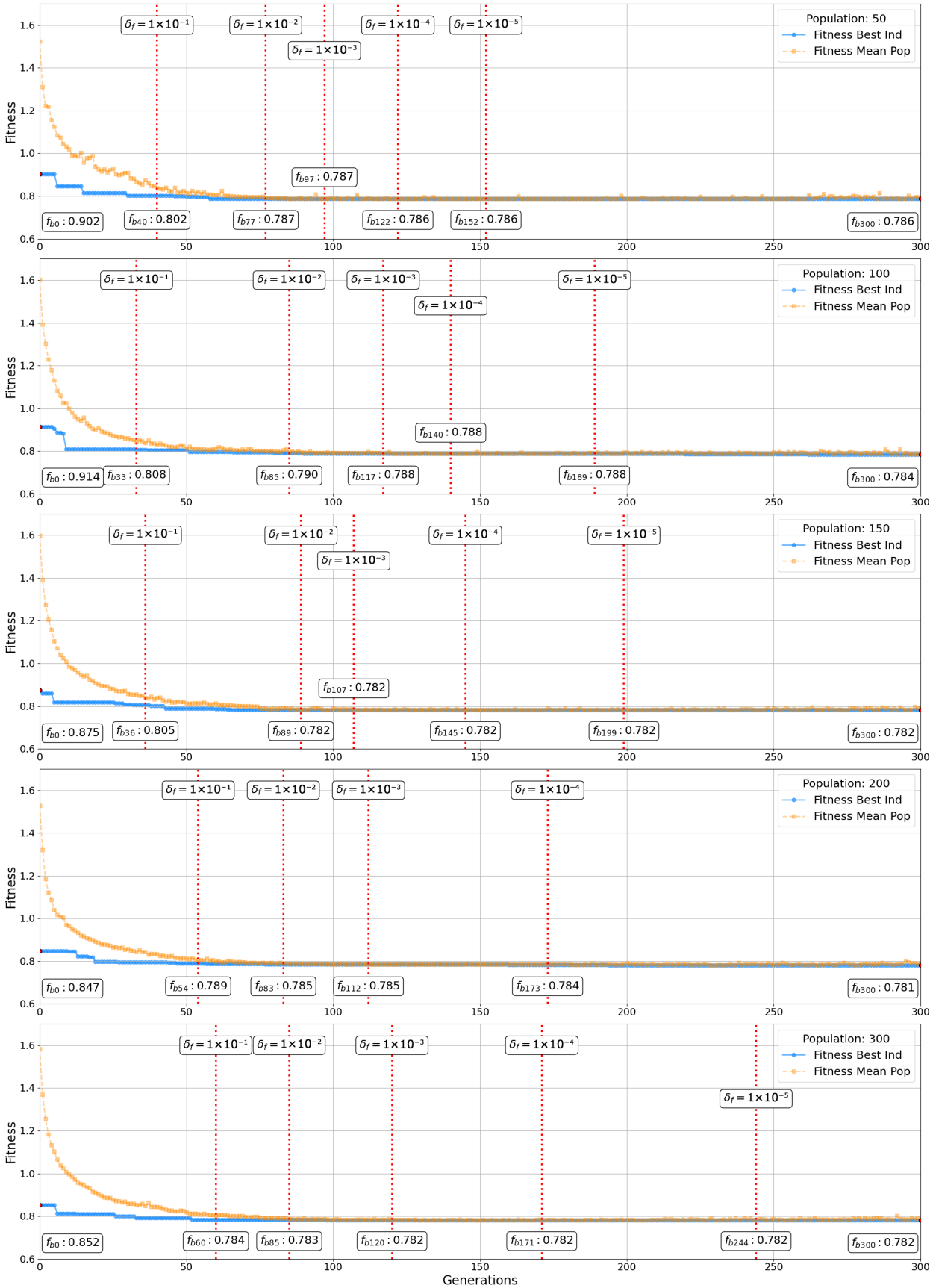


Figure 7. Evolution of best individual fitness f_b, the mean population fitness f_m and the delta population fitness over 300 generations for populations with different numbers of individuals and a turnover value of 20.

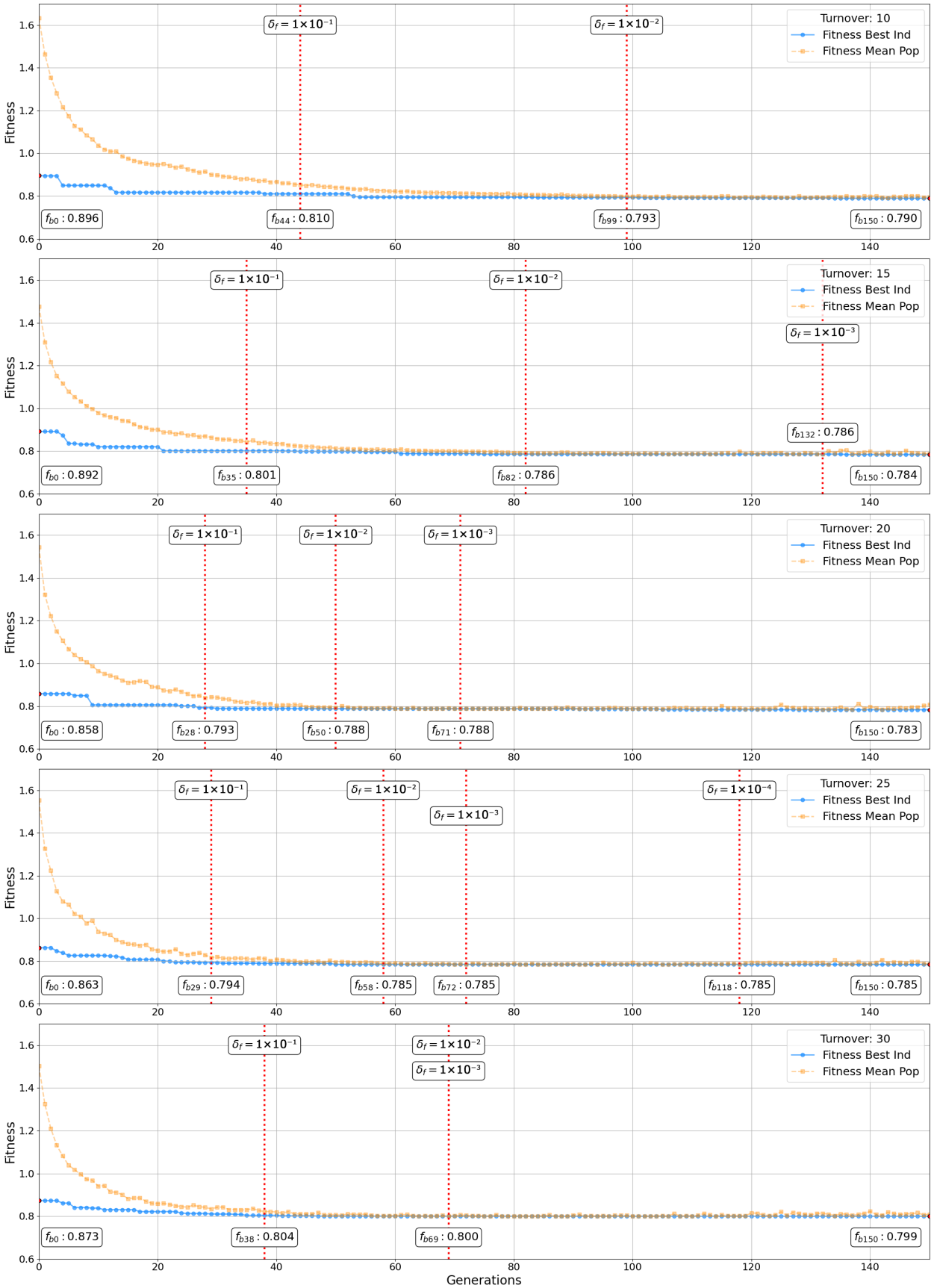


Figure 8. Evolution of average population fitness and fitness of the best individual over 150 generations for a population of 150 individuals and different turnover values.

It is important to note that for the population range analyzed for all the configurations, the best final fitness value f_{b300} varies by approximately 1%, regardless of the number of individuals in the population. This indicates that the choice of population size and turnover influences the convergence behavior of the optimization process, affecting the number of generations required to reach a converged solution and, consequently, the overall computational time.

This indicates that the choice of the individual number in the population and the number of generations mainly influence the computational time to converge to the optimal solution due to different numbers of required computations.

Figure 8 analyzes the effect of different turnover rates on the evolutionary process. The turnover is chosen in the range of 0.1–0.3, the value of population is fixed at 150 individuals and the maximum number of generations is 150.

As can be seen, the δf thresholds are reached more quickly for intermediate values, indicating convergence to the fastest optimal solution. For extreme values of sales, it can also be seen that despite the reduction in δf, the algorithm converges to a local minimum solution. This is due to the fact that the exploration within the solution space leads to lower values of δf.

This analysis shows that the influence of turnover on the value of the final best fitness f_{b150} is greater than the number of individuals in the population. Considering all the analyses performed on the configurations, the value of f_{b150} varies by about 3% depending on the turnover chosen. The turnover has a significant impact not only on the computation time but also on the solution found. It is fixed at 0.2.

Both Figures 7 and 8 show the influence of mutations on δf in the early and late generations. Increasing the probability of mutations increases the genetic variability, which prevents the algorithm from getting stuck in a local minimum. Conversely, decreasing the mutation rate in intermediate generations ensures that the focus remains on the most promising solutions. The values chosen for the extremes of the mutation rates are 0.1 and 0.01.

After choosing the above values, it is possible to set the minimum delta fitness value within the population, which is set to 10^{-4}. A larger value would reduce the computation time, but would lead to an overly early solution, negating the effect of reactivating the mutation rate. Conversely, a smaller value would never be reached due to the presence of mutations.

The main parameters configured for the GA used in this paper are presented in detail in Table 11.

It is important to note that the optimal identified configuration does not change for GA parameters in the neighborhood of those selected. However, the solution quality varies depending on them. If the parameters are not set correctly, the algorithm will still converge to a great solution, but not necessarily the optimal one.

Tests were also carried out with different combinations of mass and moments-of-inertia weights, from which it can be seen that increasing the weight assigned to inertia results in only a small improvement in inertia reduction, but a significant increase in mass. This effect is due to the quadratic dependence of inertia on component size, which makes it more difficult to contain without significantly affecting the overall weight of the EMA.

3.4.2. Case Study of EMA Optimal Configuration

The results of the optimization of the EMA configurations for the case study of the present work are shown in Figure 9.

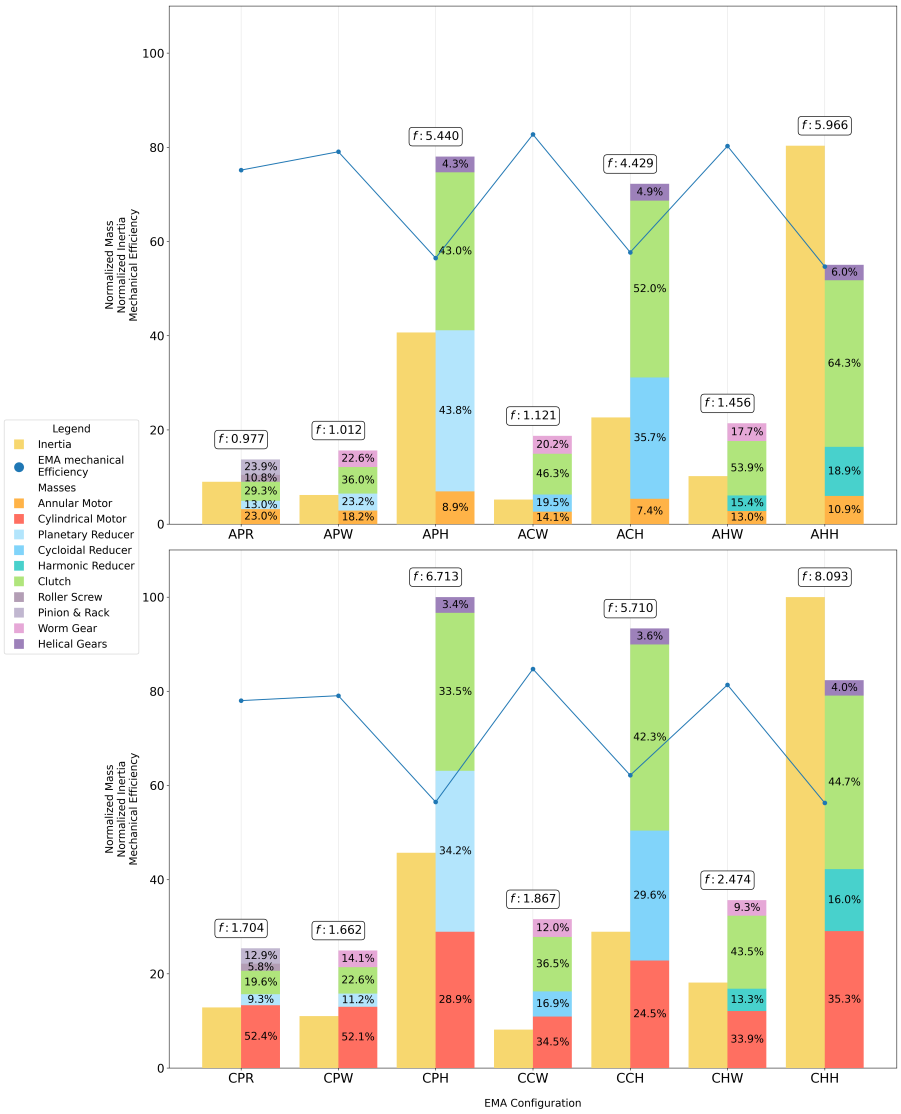


Figure 9. Comparison of mass, moment of inertia, and mechanical efficiency with electromechanical actuator configurations for the case study's optimal configurations. Required torque of 5.000 Nm and required rotational speed of 25 deg/s.

The number of configurations shown is 14 compared to the 18 analyzed, because the algorithm failed to initialize the population for the following configurations: APR, AHR, CCR, CHR. As can be seen, all of the excluded configurations involve the use of roller screws, with different combinations of motors and gearboxes. In some cases, this is due to the inability to achieve the necessary gear ratio to develop the required torque. This is because for these configurations it is not possible to find feasible solutions that accommodate both the torque and rotational speed requirements, due to the possible transmission ratio arrangements.

The EMA configurations are compared through an analysis of the mass and inertia values, both normalized with respect to the maximum value recorded among the identified solutions. The components of the configurations are indicated by the acronyms in Table 4.

The bar graphs also show the percentage distribution of the total mass among the different components, allowing the contribution of each element to the overall configuration to be assessed. This presentation helps to highlight structural differences among the solutions and to better understand the role of each component in determining the overall properties of the system.

Mechanical efficiency is reported in Figure 9, but it was not used as a selection criterion for the configuration optimization. This is due to the analyzed configurations having comparable efficiencies. Moreover, the configuration efficiency undergoes small changes with different combinations of torque and rotational speed.

From the graph, it can be seen that configurations with annular motors are lighter than their counterparts with cylindrical motors, as previously explained. The mass distribution percentage shows that for configurations with the same components except for the motor, it is the motor that negatively affects the fitness f.

By analyzing the fitness of the different configurations shown in the graph, it is clear that the optimal solution for this case study is the APR configuration, which includes an annular motor, planetary gearbox, roller screw, rack and driven gear. A representation of the chosen configuration is shown in Figure 10.

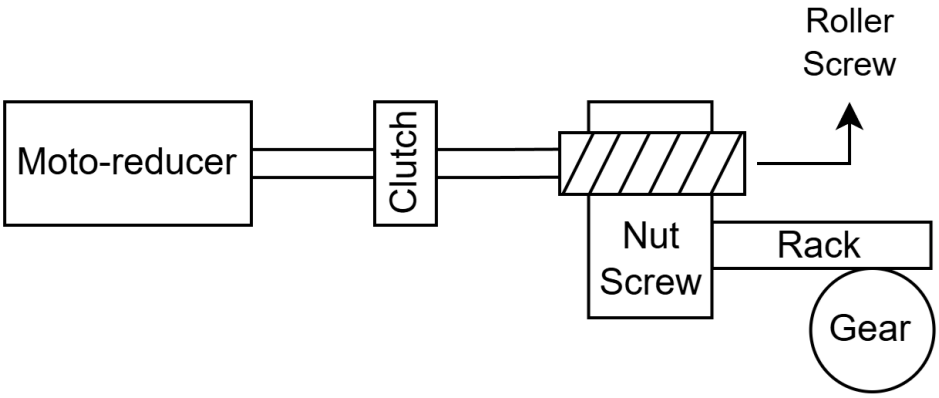


Figure 10. Schematic representation of the EMA, highlighting the transmission of motion from the motor with a gearbox to the load through a roller screw and a rack and driven gear system.

3.4.3. Optimal EMA Configuration Mapping

Beyond the identification of a single optimal solution for the case study, the proposed framework also enables a systematic exploration of how architectural preferences evolve across the torque–speed space under different design-priority assumptions. An analysis was conducted using the GA to generate a map of solutions in the space defined by the torque and speed required by the system. Since no specific application case was defined for this generalized analysis, the same values as in the case study were used for the weights assigned to the fitness-function parameters. The objective is to identify the regions in which each combination of components is optimal, thus providing a reference for selecting the most suitable configuration based on operational requirements.

Figure 11 shows the division of the torque–speed space into their respective characteristic regions.

The analysis shows how the solutions vary as the torque–speed requirements change. The acronyms indicate the type of architecture chosen, with the abbreviation of the EMA components described in Table 4.

The dominant motor within the identified solutions is the annular motor. This result was to be expected, as the annular motor has a lower exponential coefficient for the mass SL with respect to the cylindrical motor, as can be seen in Table 5.

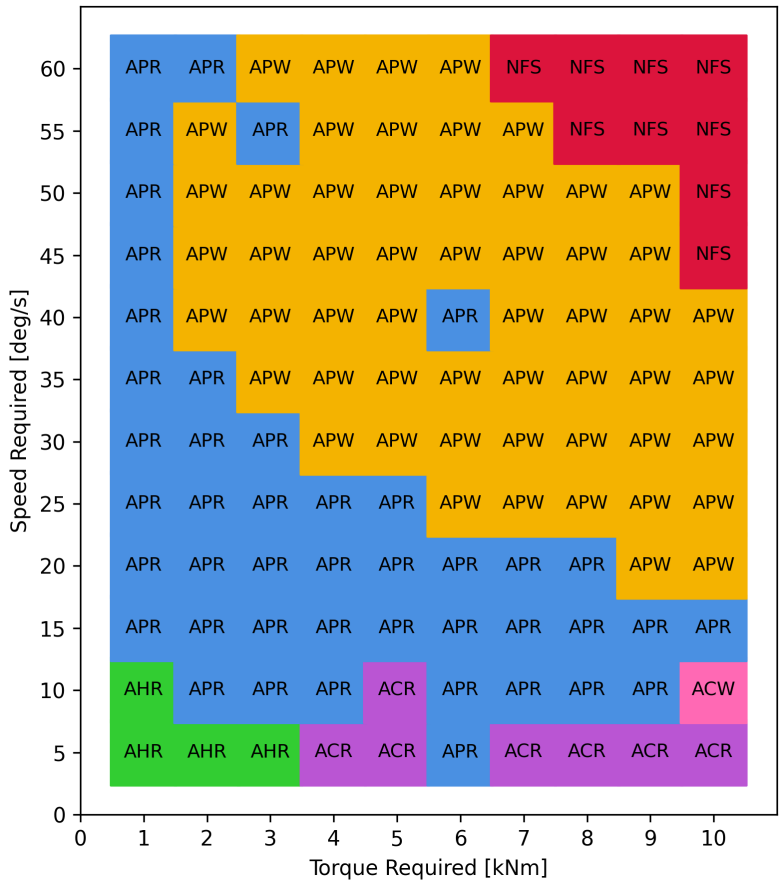


Figure 11. Map of optimal EMA configurations in torque–velocity space. APR: Annular–Planetary–Roller Screw; APW: Annular–Planetary–Worm Gear; AHR: Annular–Harmonic–Roller Screw; ACR: Annular–Cycloidal–Roller Screw; ACW: Annular–Cycloidal–Worm Gear; NFS: No Feasible Solution.

The planetary gearbox is dominant among solutions requiring higher speeds with varying torque. This is due to the greater range of possible gear ratios of the multistage planetary gears, which allows for a lower mass and total inertia on the motor side. With a higher gear ratio, it is possible to reduce the size of the electric motor, while still increasing the sizes of the clutch and transmission. Conversely, with lower gear ratios, the same torque can be obtained with higher electric motor and transmission sizes, but with greatly reduced clutch sizes. This can be observed in Figure 9. In addition, the rotational speed at the output of the planetary gearbox tends to be higher than that of the other types at the same transmitted torque. For applications with low speed, both the harmonic gearbox for non-excessive torques and the cycloidal gearbox for intermediate and high torques become competitive. In particular, harmonic gears are more suitable for lower-torque solutions, while cycloidal gears are suitable for higher torques. The reason is that for the same gear ratio, planetary gears are heavier, and since high rotational speed is not required, lower gear ratios are sufficient. In particular, harmonic gears are more suitable for lower-torque solutions, while cycloidal gears are suitable for higher torques. This is because a lower mass SL correction coefficient is assigned to cycloidal compared to harmonic gearboxes, resulting in lighter cycloidal gears for high torques and vice versa.

Regarding the type of transmission, a clear boundary can be observed between the regions dominated by roller screws and those dominated by worm gears. Looking at the coefficients of the two components in Tables 8 and 9, it is evident that the roller screws have a higher exponent for the SL of mass. This means that for lower torque, the roller screws present lower mass. The behavior of inertia is opposite for these components, but

this is combined with the fact that in the fitness calculation, the contribution of inertia is far lower than that of mass. As a result, in the lower part of the curve, architectures with roller screws are preferred, while in the upper part, those with worm gears are most suitable. No architectures with helical gears appear among the optimal solutions, since the parameters considered allow much lower gear ratios than those of the other components, and helical gears negatively affect the size of the other components, making them less favorable. This can be seen in Figure 9.

Of particular note is the isolated APR solution for a steering torque value of 6 kNm and a speed of 40 deg/s. For this point, the fitness values of the optimal solutions produced by APW and APR differ by less than $5 \cdot 10^{-4}$. This outcome can be explained by the fact that the optimal APR solution incorporates a planetary gearbox with a smaller size, and consequently lower mass and inertia, compared to the APW configuration. Specifically, the planetary gearbox of the APR configuration has the highest reduction ratio with only one reduction stage, while the APW configuration has the lowest reduction ratio with two reduction stages, increasing its mass. A similar behavior can also be observed in the neighboring requirement combinations, where APR remains competitive despite APW being generally dominant in the surrounding region.

There are also areas marked NFS, where the GA did not find any feasible solution. This indicates combinations of torque and speed that fall outside the feasible operating range of the available components considered in the analysis.

Building on the mapping of optimal configurations, the GA is applied to the specific case study characterized by the aircraft data in Table 2 and the requirements in Table 3.

Building on the configuration mapping presented in Figure 11, an additional analysis was conducted to investigate the influence of the weighting coefficients adopted in the fitness function on the identified optimal EMA architectures.

As discussed in Section 3.4.1, the weighting factors associated with mass and equivalent inertia represent design priorities rather than intrinsic physical properties, and their selection is inherently application-dependent. In practical design applications, the selection of weighting coefficients would be driven by system-level requirements, such as control bandwidth, transient response, or stability margins, and would typically be refined as the design process progresses and higher-fidelity models become available. In the absence of explicit higher-level system requirements for the generalized torque–speed characteristics, the weighting factors are therefore used to explore alternative design scenarios and to highlight how changes in priority influence the relative competitiveness of different EMA architectures.

To this end, two additional optimization campaigns were performed using alternative weight combinations: an equal-weight case ($w_m = 0.5$, $w_j = 0.5$) and an inertia-prioritized case ($w_m = 0.2$, $w_j = 0.8$). The resulting configuration maps are reported in Figure 12a and Figure 12b, respectively, and are directly comparable with the baseline map obtained using $w_m = 0.8$, $w_j = 0.2$.

A first relevant observation is that the overall structure of the solution space remains qualitatively consistent across all weighting scenarios. The dominant motor topology continues to be the annular motor, and the main transitions between reducer and transmission technologies occur along comparable torque–speed boundaries. This indicates that the optimization outcomes are primarily driven by the underlying scaling laws and feasibility constraints, rather than being arbitrarily dictated by the chosen weighting coefficients.

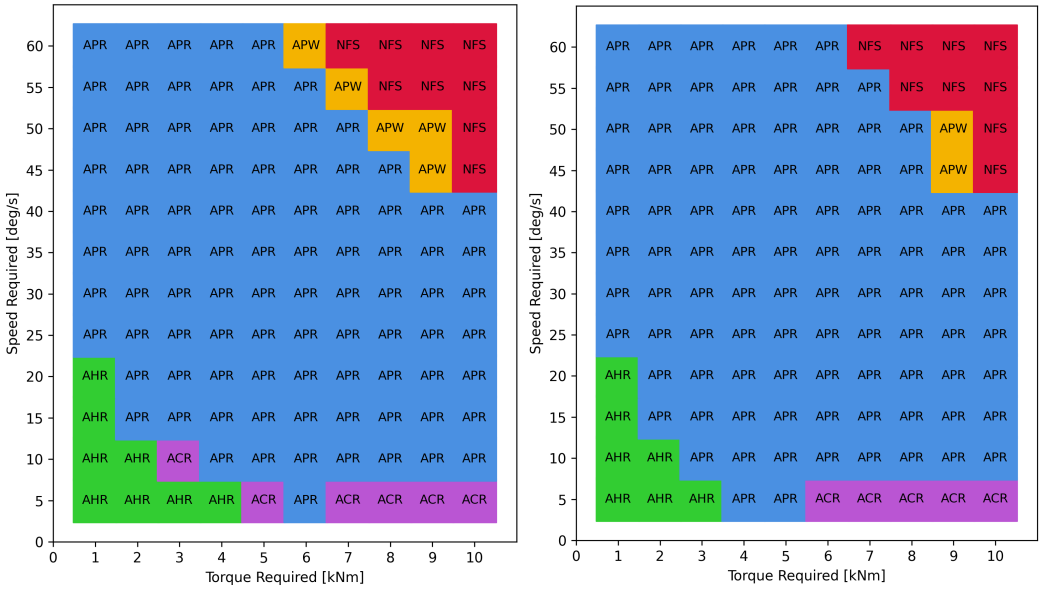


Figure 12. Map of optimal EMA configurations in torque–velocity space for different masses and inertia weights: (**a**) $w_m = 0.5$ and $w_j = 0.5$; (**b**) $w_m = 0.2$ and $w_j = 0.8$. APR: Annular–Planetary–Roller Screw; APW: Annular–Planetary–Worm Gear; AHR: Annular–Harmonic–Roller Screw; ACR: Annular–Cycloidal–Roller Screw; NFS: No Feasible Solution.

Nevertheless, noticeable quantitative differences emerge in the relative extent of the regions associated with specific architectures. In both alternative weighting cases, the region corresponding to the APR configuration expands and partially replaces areas previously dominated by the APW configuration in the baseline map. This behavior can be physically interpreted by considering the effect of the achievable reduction ratios on the equivalent inertia reflected at the motor shaft, which alters the distribution of size and mass along the actuation chain. The planetary reducer combined with the roller-screw-based transmission allows higher reduction ratios to be realized within feasible component limits, leading to a more effective attenuation of downstream inertial contributions.

As the weight assigned to inertia increases, this effect becomes progressively more influential in the fitness evaluation, favoring architectures capable of minimizing reflected inertia even at the expense of moderate mass penalties.

The observed behavior indicates that the optimization results are reasonably stable with respect to moderate variations in the fitness-function weighting, while remaining sensitive to changes in the relative importance assigned to mass and inertia.

3.4.4. Linear and Preliminary Non-Linear Models Analysis

In order to analyze the dynamic behavior of the EMA, the system in Figure 10 can be represented by an equivalent mechanical linear representation, as shown in Figure 13.

The components of the EMA are linearized as rotating masses, connected to each other by springs, representing the stiffness of the component. In this analysis the motor is approximated to a single-phase motor.

The equations describing the linear model are given in the system Equation (42).

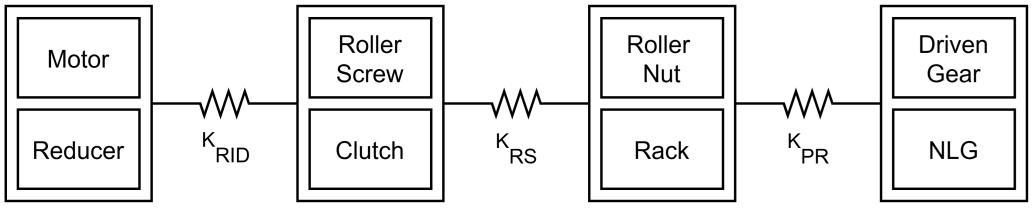


Figure 13. Equivalent mechanical model of the EMA, showing the subsystems with their respective torsional and linear stiffness for dynamic analysis of the system. k_{RID} is the equivalent torsional stiffness of the motor and gearbox, considered a single subsystem; k_{RS} is equivalent torsional stiffness of roller screw and clutch, also considered a single subsystem; k_{PR} is the equivalent linear stiffness of the roller nut and rack subsystem; the last subsystem is the rack and NLG, where NLG stands for the nose landing gear leg.

$$\begin{bmatrix} J_{RID} & 0 & 0 & 0 \\ 0 & J_{RS} & 0 & 0 \\ 0 & 0 & I_{RCK} & 0 \\ 0 & 0 & 0 & J_{NLG} \end{bmatrix} \begin{Bmatrix} \ddot{\theta}_{RID} \\ \ddot{\theta}_{RS} \\ \ddot{x}_{RCK} \\ \ddot{\theta}_{NLG} \end{Bmatrix} + \\ + \begin{bmatrix} k_{RID} & -k_{RID} & 0 & 0 \\ -k_{RID} & k_{RS}\left[\frac{R_{Rs}}{2\pi}\right]^2 + k_{RID} & -k_{RS}\left[\frac{R_{Rs}}{2\pi}\right] & 0 \\ 0 & -k_{RS}\left[\frac{R_{Rs}}{2\pi}\right] & k_{PR} + k_{RS} & -k_{PR}\left[\frac{R_{HG}}{2\pi}\right] \\ 0 & 0 & -k_{PR}\left[\frac{R_{HG}}{2\pi}\right] & k_{PR}\left[\frac{R_{HG}}{2\pi}\right]^2 \end{bmatrix} \begin{Bmatrix} \theta_{RID} \\ \theta_{RS} \\ x_{RCK} \\ \theta_{NLG} \end{Bmatrix} = 0 \quad (42)$$

The natural frequencies of the system in Equation (42) are [17632, 1989, 1183, 1033] Hz. Since these values are at least two orders of magnitude higher than the operating frequency in Table 3, resonance effects will not occur.

Considering this case study, another phenomenon must be taken into account. A common issue with the NLG is the shimmy phenomenon, an oscillation that depends on both the speed of the aircraft and the inertia characteristics of the landing gear [56]. The shimmy can occur when the aircraft travels over uneven surfaces or due to worn tires and can range from mild vibrations to severe vibrations, which can potentially lead to catastrophic failure such as NLG detachment. It is necessary to verify that the operating frequency of the EMA does not resonate with the shimmy frequency. To mitigate this risk, the NLG is often equipped with a shimmy damper, a device designed to reduce oscillations.

The dynamic behavior of the NLG during ground operations can be represented schematically as shown in Figure 14.

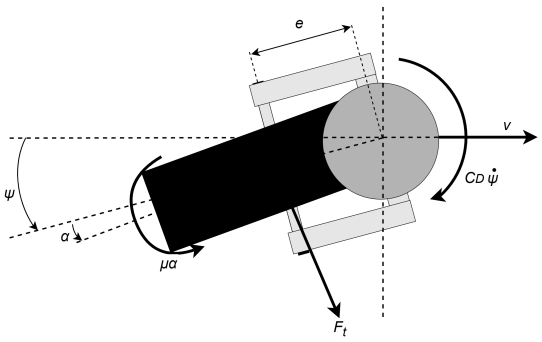


Figure 14. Schematic representation of the nose landing gear with an "L" shape in top view; presence of the slip angle α for shimmy evaluation.

In this representation, the NLG moves at the speed v. e is the caster length. Since the wheel is free to swing around the pivot, the yaw rotation angle ψ and the slip angle α define the motion of the system. μ is the torsional stiffness of the tire. C_D represents the equivalent damping coefficient. The force F_t is the force of the tread–track contact, which depends on the steering stiffness coefficient c_s. k_L represents the lateral stiffness. As already shown in Figure 4, a force $F_{z_{NLG}}$ is applied to the tire, causing it to flatten with the half-length of the contact surface a. This can be represented by the system in Equation (43).

$$\begin{bmatrix} J & 0 \\ 0 & 0 \end{bmatrix} \begin{Bmatrix} \ddot{\psi} \\ \ddot{\alpha} \end{Bmatrix} + \begin{bmatrix} C_D + \frac{0.15a^2 c_s F_{z_{NLG}}}{v} & 0 \\ ck_L e & 1 \end{bmatrix} \begin{Bmatrix} \dot{\psi} \\ \dot{\alpha} \end{Bmatrix} + \begin{bmatrix} 0 & -\frac{e}{c} - \mu \\ ck_L & ck_L v \end{bmatrix} \begin{Bmatrix} \psi \\ \alpha \end{Bmatrix} = \begin{Bmatrix} 0 \\ 0 \end{Bmatrix} \tag{43}$$

By analyzing the system Equation (43) it is possible to determine the frequencies at which shimmy may occur [57]. Taking into consideration a variable aircraft speed, as it changes, it is possible to obtain a curve representing the shimmy frequency band, as shown in Figure 15.

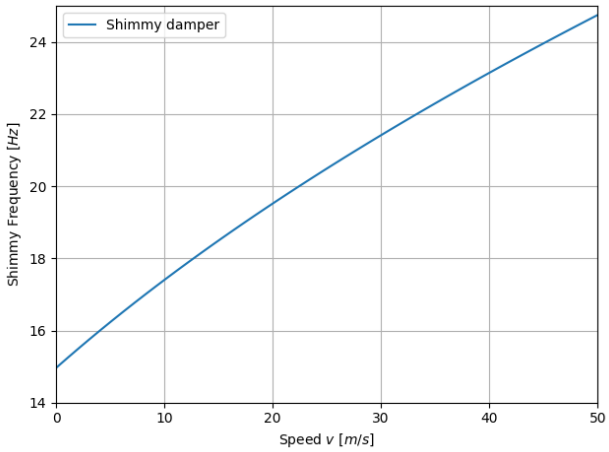


Figure 15. Shimmy frequency analysis with varying aircraft cruising speed.

Depending on the aircraft speed, the shimmy frequency can vary in the range of 15–25 Hz. Previous studies present similar results, placing the frequency band of the shimmy phenomenon between 10 and 30 Hz, validating the results obtained [41,58].

Having verified that the shimmy frequency band is lower than the natural frequencies of the steering system obtained with Equation (42), the proper system operation can be verified by using a position controller with nested rotational speed and current loops.

The controlled position corresponds to the commanded angular displacement and is implemented using a proportional (P) controller, while proportional–integrative (PI) controllers are employed for the regulation of rotational speed and current.

Feedback signals are acquired through transducers of varying dynamic orders. A zero-order transducer is used for position measurement, as a simplification of a rotary variable differential transformer. Velocity feedback is provided by a first-order transducer, serving as a simplified approximation of a resolver. Current measurement is modeled using a second-order transducer, corresponding to an idealized form of a current transformer.

This ensures a faster response and suitable performance while preserving system stability. Figure 16 shows the Bode plots of controller magnitudes and phases.

The controllers is tuned such that the current loop cutoff frequency does not exceed the electrical limit imposed by the motor's electric characteristics. The position loop cutoff frequency must be greater than the required specification in Table 3. The parameters are also tuned so that the cutoff frequency of the speed loop is about halfway between the others.

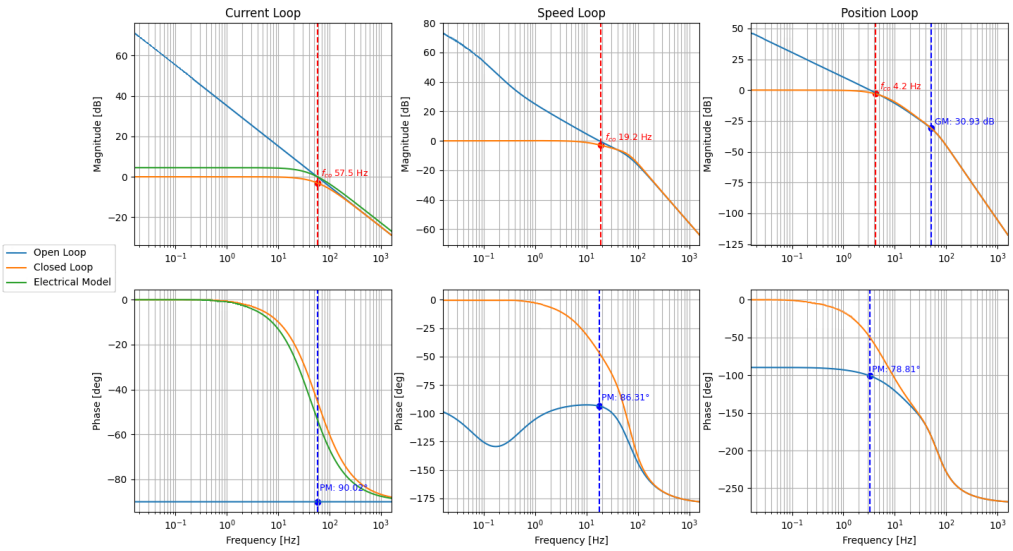


Figure 16. Bode diagrams of current, speed and position loops of the position controller, with nested speed and current loops.

Following the controller parameter tuning, a preliminary non-linear model can be developed. This model includes the controller described above, with the addition of the saturation imposed by the selected motor. The motor is simplified and modeled as a DC motor, the transmission components are shown as in Figure 13, and the NLG friction force model described above is developed to verify the force.

Figure 17 shows the dynamic response to a 45 deg step position input for the non-linear model, without an external load. The step signal is equal to the maximum steering angle allowed during taxing maneuvers.

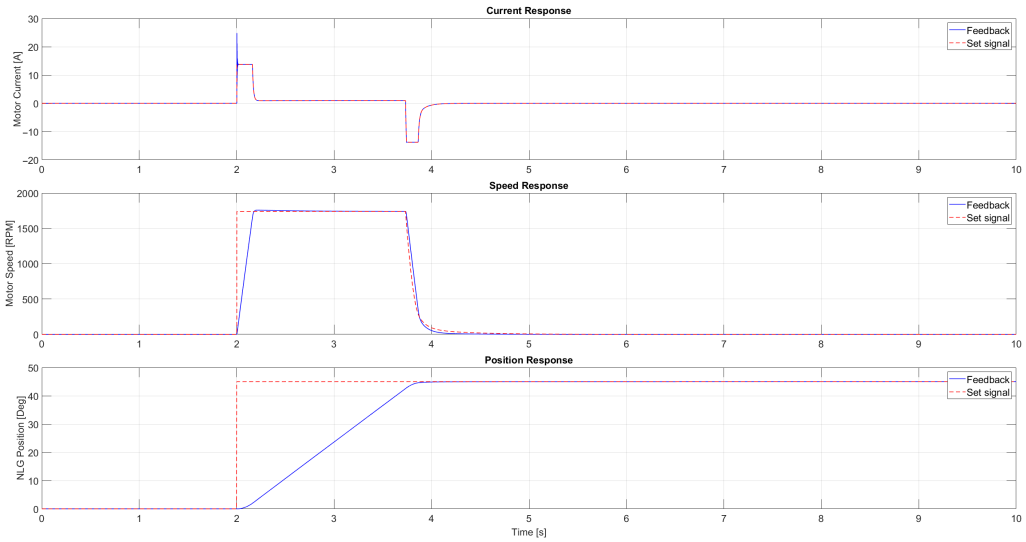


Figure 17. Preliminary non-linear model time response for a step position input corresponding to the maximum allowable NLG position angle in taxing operations.

As can be seen, the current and speed responses are fast enough to match their set signals, according to the controller parameter tuning. This analysis makes it possible to evaluate the maximum rotation speed of the NLG. It corresponds to 25.87 deg/s, which is greater than the requirement in Table 3.

Figure 18 shows an example of an aircraft taxing operation. The maneuver is performed at the maximum speed allowed by the NLG and with a steering angle within the

range specified in Table 3. A disturbance torque is also applied, in accordance with the model described in Section 3.1.

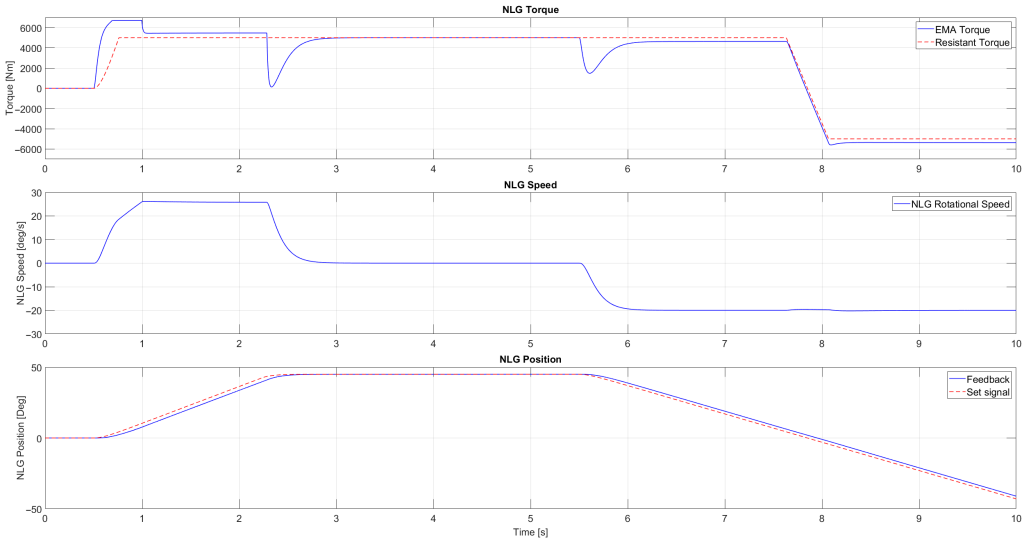


Figure 18. Preliminary non-linear model time response for a taxing operation: the input corresponds to the maximum rotational speed, until the maximum permitted angle is reached; the reverse maneuver is then performed.

As can be seen, in addition to the rotational speed requirement, the torque requirement is also satisfied. In particular, the EMA is capable of generating a torque of 6500 Nm, which is higher than the requirement in Table 3.

Finally, a chirp signal can be used to verify that the EMA can also meet the frequency response requirement for the landing and take-off operations. Figure 19 shows the application of a chirp signal with an incremental frequency from 0.1 Hz to 4.2 Hz, with a fixed amplitude of 1.5 deg.

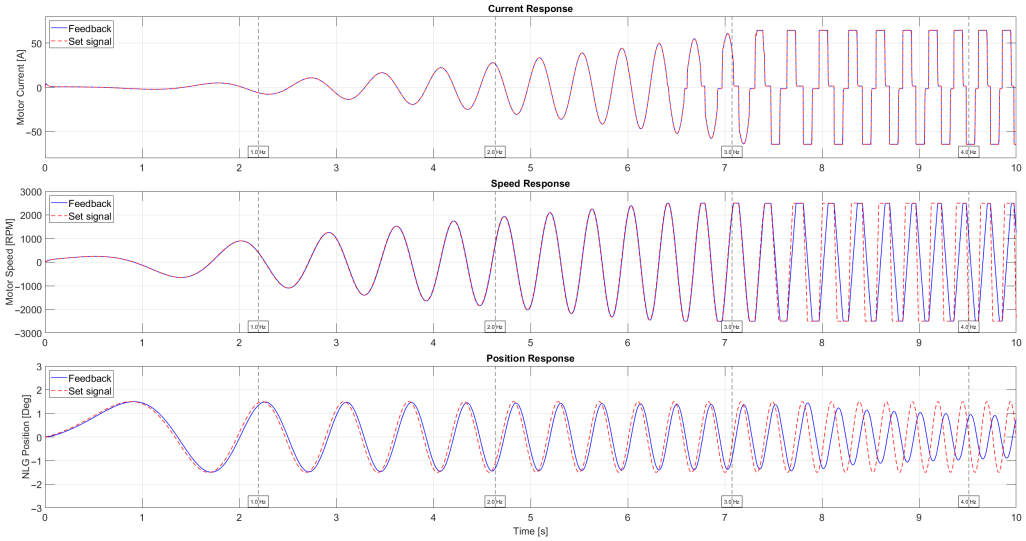


Figure 19. Preliminary non-linear model time response for a chirp (0.1–4.2 Hz) position input with an amplitude of 1.5 deg.

The position feedback, although slightly delayed, has an acceptable response, with an attenuation of about 30% at 4 Hz. Therefore, the frequency response requirement in Table 3 is verified for a signal with maximum amplitude equal to the maximum angle during take-off and landing phases, also shown in Table 3.

The characteristics of the designed APR-EMA shown in this section are listed and compared with the requirements of the case study in Table 12.

Table 12. Comparison between the requirements imposed in genetic algorithm for optimal EMA configuration identification and the characteristics of the identified and designed APR-EMA.

Symbol	Parameter	Requirement	Designed	Unit
T_{NLG}	Required steering torque	5.000	6.500	Nm
θ_{tax}	Taxing NLG steering angle	± 45	± 45	deg
$\theta_{lan/toff}$	Landing and take-off NLG steering angle	± 1.5	± 1.5	deg
ω_{min}	Minimum NLG steering speed	25	25.87	deg/s
f_{EMA}	Position cutoff frequency	4	4.2	Hz

4. Summary

This paper presents a novel and systematic framework for the early-stage design and optimization of electromechanical actuators (EMAs), with particular relevance to aerospace applications. The key achievements can be summarized as follows:

- Integrated preliminary design methodology: This paper presents a novel and systematic framework for the early-stage design and optimization of electromechanical actuators (EMAs), with particular relevance to aerospace applications. The proposed workflow integrates system-level requirements, component-level scaling laws, and architecture selection within a single optimization framework, enabling consistent and traceable EMA sizing from the earliest design phases.
- Custom genetic algorithm for non-convex, multi-architecture optimization: A tailored genetic algorithm is developed to handle multiple EMA architectures and several design variables, including strict compatibility and constraint checks along the electromechanical chain. This allows a robust exploration of feasible solutions in highly non-convex design spaces, where traditional gradient-based methods would fail.
- Application and validation on a realistic aerospace case study: The proposed methodology is applied to the nose landing gear steering system of a transport aircraft, demonstrating its capability to identify the optimal EMA architecture under realistic operational requirements.
- Dynamic validation of optimized solutions: Linear and non-linear dynamic analyses are performed to confirm that the optimized EMA configurations satisfy stability and control requirements, showing that the early-stage optimization does not compromise system-level dynamic behavior.
- Reduction in downstream design effort: By providing well-balanced and dynamically consistent preliminary designs, the proposed framework reduces the need for extensive redesign in later development stages, thereby lowering overall development time and computational cost.

5. Conclusions and Future Developments

The objective of this article is to present a workflow for the preliminary design of an actuator, from the perspective of mass and moment-of-inertia optimization.

Starting from the definition of system requirements, a systematic identification and selection of the EMA components of interest can be performed by considering different families of motors, gearboxes, etc., depending on the intended actuator application. Within this framework, the proposed methodology provides a structured approach to support the early design phase, enabling the evaluation and comparison of alternative component typologies while targeting mass and inertia optimization.

The workflow is based on the definition of SLs for the selected components and on the use of a custom GA. The algorithm includes compatibility checks among the components and with the assigned system specifications, enabling a consistent comparison of different configurations and the identification of an optimal solution for the defined requirements.

The proposed approach has been applied to a case study involving the steering system of the Douglas DC-6. In this application, the steering torque requirement was derived from the NLG assembly and from the friction force generated by ground contact. Based on the optimization results, the configuration that includes an annular motor, planetary reducer, roller screw, rack and gear was identified as the optimal solution for the considered operating conditions.

The selection of the weights associated with mass and inertia in the fitness function has a direct influence on the GA optimization process and on the resulting optimal configuration. To analyze this effect, a sensitivity analysis on fitness-function weights was conducted to generate a set of solution maps as a function of required steering torque and rotational speed.

The configuration identified for the case study was subsequently implemented using a linear model to preliminary verify the frequency response requirements and was then extended to a preliminary non-linear model to evaluate its time-domain performance.

Finally, it is important to note that the steering system case study was adopted for illustrative purposes and represents only one practical application of the proposed workflow within a realistic design problem. The methodology can be extended to the preliminary design of different types of actuators, including non-electromechanical solutions.

With respect to system modeling, the preliminary non-linear model adopted in this work can be further extended toward higher-fidelity formulations in order to verify the obtained design under more realistic operating conditions. Moreover, the detailed actuator model could be integrated into a more comprehensive system-level model, enabling the evaluation of the EMA behavior within representative operational scenarios of the real system.

As stated above, the proposed workflow is focused on the optimization of EMA mass and moment of inertia, while some system-level requirements are not explicitly addressed. Among these, the verification of accuracy requirements represents a relevant limitation of the current framework. For applications in which positioning or tracking accuracy constitutes a system requirement, the integration of accuracy-related metrics within the GA, either as feasibility constraints or as additional optimization objectives, would represent a natural extension of the proposed methodology.

In addition to accuracy, safety and reliability aspects of the resulting configurations are not explicitly considered. Although not included in the current formulation, safety and reliability assessments should be regarded as a necessary step in the component selection process. A possible and relevant future development consists of the integration of safety and reliability analyses within the GA framework, with the objective of reducing the number of external preliminary evaluation steps required when applying the workflow. These analyses could be incorporated either as feasibility checks, by imposing threshold criteria on the admissibility of a given architecture, for instance, based on a maximum acceptable failure rate, or as additional optimization objectives, by including reliability maximization within the fitness function.

A further potential enhancement of the proposed methodology is the evaluation and minimization of the overall EMA dimensions. As in the case of accuracy, safety, and reliability, configurations that are optimal in terms of mass and moment of inertia do not necessarily satisfy dimensional constraints, which may represent a system-level require-

ment in several applications. For this reason, the automation of the overall dimensional assessment within the GA represents an interesting direction for future implementations.

Author Contributions: Conceptualization, M.L., A.C.B., R.G. and D.F.M.; data curation, M.L.; formal analysis, M.L., A.C.B. and R.G.; funding acquisition, M.S.; investigation, M.L.; methodology, M.L.; project administration, A.C.B. and D.F.M.; resources, A.C.B.; software, M.L.; supervision, A.C.B., D.F.M. and M.S.; validation, M.L., A.C.B., R.G., D.F.M. and E.F.; visualization, M.L.; writing—original draft, M.L.; writing—review and editing, M.L., A.C.B., R.G. and E.F. All authors have read and agreed to the published version of the manuscript.

Funding: This publication is part of the project PNRR-NGEU, which has received funding from the MUR–DM 352/2022. This research is co-funded by Leonardo S.p.A.

Institutional Review Board Statement: Not applicable.

Informed Consent Statement: Not applicable.

Data Availability Statement: Data are contained within the article.

Conflicts of Interest: Authors Domenico Fabio Migliore and Edoardo Finamore were employed by the company Leonardo S.p.A. The remaining authors declare that the research was conducted in the absence of any commercial or financial relationships that could be construed as a potential conflict of interest.

References

1. Balaban, E.; Saxena, A.; Bansal, P.; Goebel, K.F.; Curran, S. A Diagnostic Approach for Electro-Mechanical Actuators in Aerospace Systems. In Proceedings of the 2009 IEEE Aerospace Conference, Big Sky, MT, USA, 7–14 March 2009.
2. Behbahani, A.R.; Semega, K.J. *Control Strategy for Electro-Mechanical Actuators Versus Hydraulic Actuation Systems for Aerospace Applications*; Technical Report; SAE International: Warrendale, PA, USA, 2018. [CrossRef]
3. Maré, J.C.; Budinger, M. Comparative analysis of energy losses in servo-hydraulic, electro-hydrostatic and electro-mechanical actuators. In Proceedings of the 11th Scandinavian International Conference on Fluid Power, SICFP'09, Linköping, Sweden, 2–4 June 2009.
4. Dell'Amico, A.; Reichenwallner, C. A Conceptual Comparison of Hydraulic and Electric Actuation Systems for a Generic Fighter Aircraft. *Aerospace* **2025**, *12*, 1. [CrossRef]
5. Moerman, F. 21-Hygienic supply of electricity in food factories. In *Hygienic Design of Food Factories*, 2nd ed.; Holah, J., Lelieveld, H.L., Moerman, F., Eds.; Woodhead Publishing Series in Food Science, Technology and Nutrition; Woodhead Publishing: Sawston, UK, 2023; pp. 485–529. [CrossRef]
6. Girinon, S.; Baumann, C.; Piquet, H.; Roux, N. Analytical modeling of the input admittance of an electric drive for stability analysis purposes. *Eur. Phys. J.-Appl. Phys.* **2009**, *47*, 11101. [CrossRef]
7. Shi, Z.; Zhang, P.; Lin, J. High performance control method of electro-mechanical actuator based on active disturbance rejection control. *Adv. Mech. Eng.* **2022**, *14*, 16878132221114189. [CrossRef]
8. Liscouët, J.; Maré, J.C.; Orieux, S. Automated generation selection and evaluation of architectures for electromechanical actuators. In Proceedings of the 26th International Congress of the Aeronautical Sciences, Anchorage, Alaska, USA, 4–19 September 2008.
9. Liscouët, J.; Maré, J.C.; Budinger, M. An integrated methodology for the preliminary design of highly reliable electromechanical actuators: Search for architecture solutions. *Aerosp. Sci. Technol.* **2012**, *22*, 9–18. [CrossRef]
10. Budinger, M.; Liscouet, J.; Stephane, O.; Budinger, M.; Liscouet, J.; Orieux, S.; Maré, J.C. Automated preliminary sizing of electromechanical actuator architectures. *Variations* **2008**, *3*, 1–6.
11. Budinger, M.; Liscouët, J.; Hospital, F.; Maré, J.C. Estimation models for the preliminary design of electromechanical actuators. *Proc. Inst. Mech. Eng. Part G J. Aerosp. Eng.* **2012**, *226*, 243–259. [CrossRef]
12. Li, W.; Fielding, J.P. Preliminary Study of EMA Landing Gear Actuation. In Proceedings of the 28th International Congress of the Aeronautical Sciences, Brisbane, Australia, 23–28 September 2012.
13. Giampaolo, B.D.; Iannaccone, G.; Lerro, A. Preliminary Design of an Actuation System for a Morphing Winglet. In Proceedings of the 2017 8th International Conference on Mechanical and Aerospace Engineering, Prague, Czech Republic, 22–25 July 2017.
14. Richiedei, D. Integrated selection of gearbox, gear ratio, and motor through scaling rules. *Mech. Based Des. Struct. Mach.* **2018**, *46*, 712–729. [CrossRef]
15. Maré, J.C. A Preliminary Top-Down Parametric Design of Electromechanical Actuator Position Control. *Aerospace* **2022**, *9*, 314. [CrossRef]

16. Reichert, T.; Nussbaumer, T.; Kolar, J.W. Torque Scaling Laws for Interior and Exterior Rotor Permanent Magnet Machines. Technical Report. In Proceedings of the IEEE International Magnetics Conference (INTERMAG), Sacramento, CA, USA, 4–8 May 2009.
17. Saerens, E.; Crispel, S.; García, P.L.; Verstraten, T.; Ducastel, V.; Vanderborght, B.; Lefeber, D. Scaling laws for robotic transmissions. *Mech. Mach. Theory* **2019**, *140*, 601–621. [CrossRef]
18. Saerens, E.; Crispel, S.; Garcia, P.L.; Ducastel, V.; Beckers, J.; Winter, J.D.; Furnemont, R.; Vanderborght, B.; Verstraten, T.; Lefeber, D. Scaling laws for parallel motor-gearbox arrangements. In *Proceedings of the IEEE International Conference on Intelligent Robots and Systems*; Institute of Electrical and Electronics Engineers Inc.: New York, NY, USA, 2020; Volume 10, pp. 6339–6346. [CrossRef]
19. Pardalos, P.M.; Žilinskas, A.; Žilinskas, J. *Probabilistic Bounds in Multi-Objective Optimization*; Springer International Publishing: Cham, Switzerland, 2017; Volume 123. [CrossRef]
20. Qiao, G.; Liu, G.; Shi, Z.; Wang, Y.; Ma, S.; Lim, T.C. A review of electromechanical actuators for More/All Electric aircraft systems. *Proc. Inst. Mech. Eng. Part C J. Mech. Eng. Sci.* **2018**, *232*, 4128–4151. [CrossRef]
21. Rosero, J.A.; Ortega, J.A.; Aldabas, E.; Romeral, L. Moving towards a more electric aircraft. *IEEE Aerosp. Electron. Syst. Mag.* **2007**, *22*, 3–9. [CrossRef]
22. Van den Bossche, D. A380 Primary Flight Control Actuation System. 2001. Available online: https://r3asc14.sciencesconf.org/conference/r3asc14/pages/R3ASC_summary_1998_2001_2004_2007_2010_2012_30Nov13.pdf?utm_source=chatgpt.com (accessed on 1 January 2025).
23. Bertolino, A.C.; De Martin, A.; Jacazio, G.; Sorli, M. A technological demonstrator for the application of PHM techniques to electro-mechanical flight control actuators. In Proceedings of the 2022 IEEE International Conference on Prognostics and Health Management (ICPHM), Detroit, MI, USA, 6–8 June 2022; pp. 70–76. [CrossRef]
24. Todeschi, M. Airbus—EMAs for flight controls actuation system—An important step achieved in 2011. In *Proceedings of the SAE Technical Papers*; SAE Internationall: Warrendale, PA, USA, 2011. [CrossRef]
25. Chevalier, P.Y.; Grac, S.; Liegois, P.Y. More Electrical Landing Gear Actuation Systems. 2010. Available online: https://r3asc16.sciencesconf.org/conference/r3asc16/pages/R3ASC_summary_1998_2001_2004_2007_2010_2012_2014_15may14.pdf?utm_source=chatgpt.com (accessed on 1 January 2025).
26. Cowan, J.R.; Weir, R.A. *Design and Test of Electromechanical Actuators for Thrust Vector Control*; Technical Report; National Aeronautics and Space Administration Marshall Space Flight Center: Huntsville, AL, USA, 1992.
27. Vanthuyne, T. An Electrical Thrust Vector Control System for the Vega Launcher. In Proceedings of the 13th European Space Mechanisms and Tribology Symposium, Vienna, Austria, 23–25 September 2009.
28. Iordanidis, G.; Bagnall, L.; Morris, J.; Grac, S.; Messier-Bugatt, E.C.; Mare, J.C.; Ivanov, S.; Basset, M.; Lauffenburger, J.P.; Pouly, G. An Overview of Modelling and Simulation Activities for an All-Electric Nose Wheel Electric System. In Proceedings of the 4th International Conference on Recent Advances in Aerospace Actuation Systems and Components, Toulouse, France, 5–7 May 2010.
29. Bennett, J.W.; Mecrow, B.C.; Atkinson, D.J.; Maxwell, C.; Benarous, M. A Fault Tolerant Electric Drive for an Aircraft Nose Wheel Steering Actuator. *IET Electr. Syst. Transp.* **2011**, *1*, 117–125. [CrossRef]
30. Zhang, M.; Li, C.; Wu, X.; Zhu, Y. All-Electric Aircraft Nose Wheel Steering System with Two Worm Gears. *Trans. Nanjing Univ. Aeronaut. Astronaut.* **2018**, *35*, 170–180.
31. Jufer, M. *Electromécanique*; Presses Polytechniques et Universitaires Romandes: Lausanne, Switzerland, 1995; Volume IX.
32. Mikhalevich, V.; Gupal, A.; Norkin, V. *Methods of Nonconvex Optimization (English Version);* Nauka: Moscow, Russia, 2024; pp. 205–206.
33. Deb, K.; Jain, S. Multi-speed gearbox design using multi-objective evolutionary algorithms. *J. Mech. Des.* **2003**, *125*, 609–619. [CrossRef]
34. Buiga, O.; Tudose, L. Optimal mass minimization design of a two-stage coaxial helical speed reducer with Genetic Algorithms. *Adv. Eng. Softw.* **2014**, *68*, 25–32. [CrossRef]
35. Bhoskar, T.; Kulkarni, O.K.; Kulkarni, N.K.; Patekar, S.L.; Kakandikar, G.M.; Nandedkar, V.M. *Genetic Algorithm and Its Applications to Mechanical Engineering: A Review*; Elsevier Ltd.: Amsterdam, The Netherlands, 2015; Volume 2, pp. 2624–2630. [CrossRef]
36. Kramer, O. *Genetic Algorithm Essentials*; Studies in Computational Intelligence; Springer: Cham, Switzerland, 2017; Volume 679. [CrossRef]
37. Blickle, T.; Thiele, L. *A Comparison of Selection Schemes Used in Genetic Algorithms*; ETH Zurich: Zurich, Switzerland, 1995.
38. Eiben, A.E.; Smith, J.E. *Introduction to Evolutionary Computing*, 2nd ed.; Springer: Berlin/Heidelberg, Germany, 2003.
39. Eshelman, L.J.; Schaffer, J.D. Real-Coded Genetic Algorithms and Interval-Schemata. In Proceedings of the Foundations of Genetic Algorithms, Vail, CO, USA, 26–29 July 1992.
40. Herrera, F.; Lozano, M.; Verdegay, J.L. Tackling Real-Coded Genetic Algorithms: Operators and Tools for Behavioural Analysis, *Artif. Intell. Rev.* **1998**, *12*, 265–319. [CrossRef]
41. Currey, N.S. *Aircraft Landing Gear Design: Principles and Practices*; American Institute of Aeronautics and Astronautics: Reston, VA, USA, 1988. [CrossRef]

42. Flugzeuginfo.net. Douglas DC-6 Data. Available online: https://www.flugzeuginfo.net/acdata_php/acdata_dc6_en.php (accessed on 1 January 2025).
43. Gudmundsson, S. *The Anatomy of the Landing Gear*; Elsevier: Amsterdam, The Netherlands, 2014; Chapter 13, pp. 547–580. [CrossRef]
44. Ferraresi, C.; Terenziano, R. *Meccanica Applicata*, 4th ed.; Clut: Trenton, NJ, USA, 2024.
45. Yang, F.; He, X.; Shen, X.; Wang, Q. Analysis of Resistance Torque of Wheeled Steering Vehicle. In *Proceedings of the IOP Conference Series: Earth and Environmental Science*; Institute of Physics Publishing: Bristol, UK, 2020; Volume 512. [CrossRef]
46. Guida, R.; Bertolino, A.C.; Martin, A.D.; Sorli, M. Comprehensive Analysis of Major Fault-to-Failure Mechanisms in Harmonic Drives. *Machines* **2024**, *12*, 776. [CrossRef]
47. Kollmorgen. Kollmorgen Frameless Motor Selection Guide. 2012. Available online: https://www.oxni.ch/Manuals/KBM%20Betriebsanleitung.pdf (accessed on 1 January 2025).
48. Spinea. *TwinSpin®-High Precision Reduction Gears and DriveSpin®-High Precision Actuators*; Spinea: Haniska, Slovakia, 2021.
49. Haumea. Planetary Drive Catalogue. 2014. Available online: https://www.haumea.com/en/products/division-planetary-drives/modular-planetary-gearboxes2 (accessed on 1 January 2025).
50. Harmonic Drive AG. *Harmonic Drive® Product World*; Harmonic Drive AG: Limburg an der Lahn, Germany, 2019.
51. VEM. Permanent Magnet Synchronous Motors for Inverter Operation. Available online: https://it.scribd.com/document/341367303/VEM-Permanent-Magnet-Motors (accessed on 1 January 2025).
52. MWM Freni Frizioni S.R.L.. *Elecromagnetic Brakes Clutches Thooth-Type Coupling*; MWM Freni Frizioni S.R.L.: Lainate, Italy, 2020.
53. Framo Morat. Catalogue Worm Gear Sets and Customised Worm Gear Sets. Available online: https://framo-morat.com/files/redaktion/framo/unternehmen/downloads-EN/Schneckenradsatzkatalog_EN_web.pdf (accessed on 1 January 2025).
54. Apex Dynamics Inc. *High Precision Rack and Pinion*; Apex Dynamics Inc.: Taichung City, Taiwan, 2024.
55. MOOG. Planetary Roller Screws. 2020. Available online: https://www.moog.com/content/dam/moog/literature/ICD/planetaryrollerscrews.pdf (accessed on 1 January 2025).
56. Carbon, C.B.D. *Analytical Study of Shimmy of Airplane Wheels*; National Advisory Committee for Aeronautics: Washington, DC, USA, 1952.
57. Girini, G.; Sasso, M. Analisi Dello Shimmy Nei Carrelli Di Atterraggio. In Proceedings of the XXXIV Convegno AIAS, Milan, Italy, 14–17 September 2005.
58. Roskam, J. *Airplane Design Part IV: Layout Design of Landing Gear and Systems*; DARcorporation: Lawrence, KS, USA, 1989.

Disclaimer/Publisher's Note: The statements, opinions and data contained in all publications are solely those of the individual author(s) and contributor(s) and not of MDPI and/or the editor(s). MDPI and/or the editor(s) disclaim responsibility for any injury to people or property resulting from any ideas, methods, instructions or products referred to in the content.